Chemical Geology 671 (2025) 122483

Contents lists available at ScienceDirect

Chemical Geology

journal homepage: www.elsevier.com/locate/chemgeo

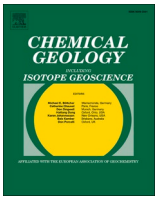

Magmatic maturation of Archean continental crust via a three-step crustal reworking, western Singhbhum Craton

Yousef Zoleikhaei [a,*], Trisrota Chaudhuri [b], Peter A. Cawood [a], Rajat Mazumder [c,d], Oliver Nebel [a,e], Shuvabrata De [f,g]

[a] School of Earth, Atmosphere and Environment, Monash University, Melbourne, Victoria 3800, Australia
[b] SIMS Laboratory, Geological Survey of India, G and IG Division, NCEGR, Kolkata 700 091, India
[c] Department of Applied Geosciences, German University of Technology in Oman, P.B. 1816, Athaiba, PC 130 Muscat, Oman
[d] Geological Studies Unit, Physics and Earth Science Division, Indian Statistical Institute, 203, B.T. Road, Kolkata 700108, India
[e] GEOMAR Helmholtz Centre for Ocean Research, Kiel, Germany
[f] College of Earth Science and Engineering, Shandong University of Science and Technology, No. 579, Qianwangang Road, Huangdao District, Qingdao 266590, China
[g] Sakariya Mines and Minerals, 1402, Ecostation Business Tower, BP Block, Salt Lake, Sector-V, Kolkata 700091, India

ARTICLE INFO

Editor: Marco Fiorentini

Keywords:
Crustal reworking
Archean
Zircon U-Pb-Hf
Bonai granite
Tamperkola granite
Singhbhum Craton

ABSTRACT

The western part of the Singhbhum Craton preserves Paleo-Mesoarchean mafic greenstone lava flows, felsic tonalite-trondhjemite-granodiorite (TTG)-granite associations, and high-K granite and volcanic suites, similar to other Archean cratonic blocks. These successions are crucial components of early continental crust, and unravelling their respective petrogenetic relations is important for understanding the evolution from mafic to felsic crust. This study presents detailed investigations of zircon U—Pb age and Hf isotope data from the Bonai TTG/gneiss-granite Suite, and the overlying Tamperkola high-K granite and rhyolite Suite. Our results indicate concurrent crystallization of the Bonai TTG gneiss (3316 ± 9 Ma), associated porphyritic high-K granite (3299 ± 9 Ma), and their amphibolite enclaves (3325 ± 9 Ma) with older, inherited zircon grains intercepting at 3586 ± 25 Ma. The entire Bonai Suite yields an overall juvenile Hf isotope composition ($\varepsilon Hf_{(t)} = -1.7$ to $+4.6$, 95 % $\varepsilon Hf_{(t)} > 0$). Combined with the mantle-like Hf isotope signatures of the inherited zircons grains ($\varepsilon Hf_{(t)} = +1.7$ to $+6.2$), this indicates a Hf isotope evolution array with a mafic crustal $^{176}Lu/^{177}Hf \approx 0.022$. Considering that these grains represent the source of the TTGs, this implies lower crustal residence of ca. 300 Myr of the mafic precursor rocks. The Tamperkola high-K magmatic suite yields a crystallization age of 2810 ± 8 Ma with sub-chondritic Hf isotope composition ($\varepsilon Hf_{(t)} = -3.2$ to -0.6). This Tamperkola Suite plots on the Hf isotope evolutionary array defined by the Bonai Suite and its mafic precursor, suggesting remelting of the Bonai (transitional) TTGs to produce these high-K granitoids in an internal reworking process. Our new and published data yield a threefold crustal evolution with (i) initial formation of the mafic crust at ca. 3586 Ma, (ii) subsequent residence for ca. 300 Myr and crustal reworking at ca. 3316–3299 Ma to form TTGs and (iii) their melting at ca. 2810 Ma to form high-K magmas. This succession of re-melting of igneous rocks drove the transition from mafic to felsic continental crust in the Singhbhum Craton. Given the consistent lithological sequence of predominantly mafic greenstone rocks, TTG-granite suites, and high-K granites observed across global cratons, this Paleo-Mesoarchean process likely reflects the order of crustal maturation in the Archean continental crust.

1. Introduction

Archean cratons preserve the oldest records of continental crust on Earth, and provide the key to unravel the development of the first continental crusts. With increasing availability of geological data from cratonic rock archives, a global pattern in the evolution of early continental crusts is being unveiled, one characterized by dominantly mafic greenstone belts and intermediate to felsic tonalite-trondhjemite-granodiorite (TTG) and late high-K granitoids, which is different from the post-Archean evolved continental crust dominated by felsic granites (e.g., Cawood et al., 2013; Hawkesworth et al., 2017; Cawood et al., 2022). However, the spatiotemporal relationships between these stage-

* Corresponding author at: School of Earth, Atmosphere and Environment, Monash University, Melbourne, Victoria 3800, Australia.
E-mail addresses: yousef.zoleikhaei@monash.edu, yousef.zoleikhaei@yahoo.com (Y. Zoleikhaei).

https://doi.org/10.1016/j.chemgeo.2024.122483
Received 2 August 2024; Received in revised form 1 November 2024; Accepted 4 November 2024
Available online 8 November 2024

specific lithological units in the Archean crustal evolution are often obscured by younger tectonic events, which has hampered our understanding of the timing and processes controlling the transition between these rock types and evolution toward modern felsic crust. For example, the occurrence of high-K granitoids in the evolving Archean crust require a pre-enrichment in K, meaning that they cannot directly form from mafic primitive crust (e.g., Laurent et al., 2014; Moyen, 2020). Their development has been taken as evidence for the maturation of cratons in the final stages of Archean orogens, and have even been linked to the melting of former surface exposed sediments (e.g., Farina et al., 2015; Reimink and Smye, 2024). However, these rocks are often spatially associated with TTGs and intermediate K-enriched rocks (transitional TTGs), and are not always associated with the end of cratonization (e.g., Barley and Pickard, 1999; Champion and Smithies, 2001; Misra et al., 2002; Belcher and Kisters, 2006; Chakraborti et al., 2019; Champion and Smithies, 2019; Hofmann et al., 2022; Rollinson et al., 2024). The persistence of these ambiguities highlights the importance of data availability from cratonic regions with relatively well-preserved and diverse lithology.

The Singhbhum Craton of eastern India preserves an extensive record of Paleo- to Neoarchean rocks related to various stages of continental crust evolution ranging from greenstone belts to TTGs and K-rich granitoids (Nelson et al., 2014; Olierook et al., 2019; Chaudhuri, 2020; Chaudhuri et al., 2022; Hofmann et al., 2022; Mazumder et al., 2022; Jodder et al., 2023). Importantly, in the western margin of the Singhbhum Craton these lithologies are in direct contact, where the mafic lavas of the Western Iron Ore Group (W-IOG) are intruded by the TTG-granite rocks of the Bonai Suite, and the Tamperkola high-K Suite intruded into the supracrustal rocks covering the Bonai Suite (Figs. 1 and 2). Recent studies reveal an early Paleoarchean age and a positive Nd isotopic composition for the Lower Lava greenstones of the W-IOG, which are interpreted to suggest melt production from a depleted mantle reservoir formed soon after planetary differentiation (Wright and Basu, 2024). Exploring petrogenetic relationships between these mantle-derived mafic rocks and the associated younger intermediate to felsic rocks can provide helpful insights on the transition from the mafic lithosphere to felsic crust on a regional scale. In this study we report magmatic zircon U—Pb age and Hf isotopes from the Bonai granitoids and their mafic enclaves and the Tamperkola high-K Suite. Our findings demonstrate that the intermediate-felsic crust is primarily generated from (partial) melting of local mafic lithosphere with contributions from older TTG crust, critically without mantle input, which then in itself matures to form high-K granites, proving the internal digestion of a protocraton to form the precursors of continental crust.

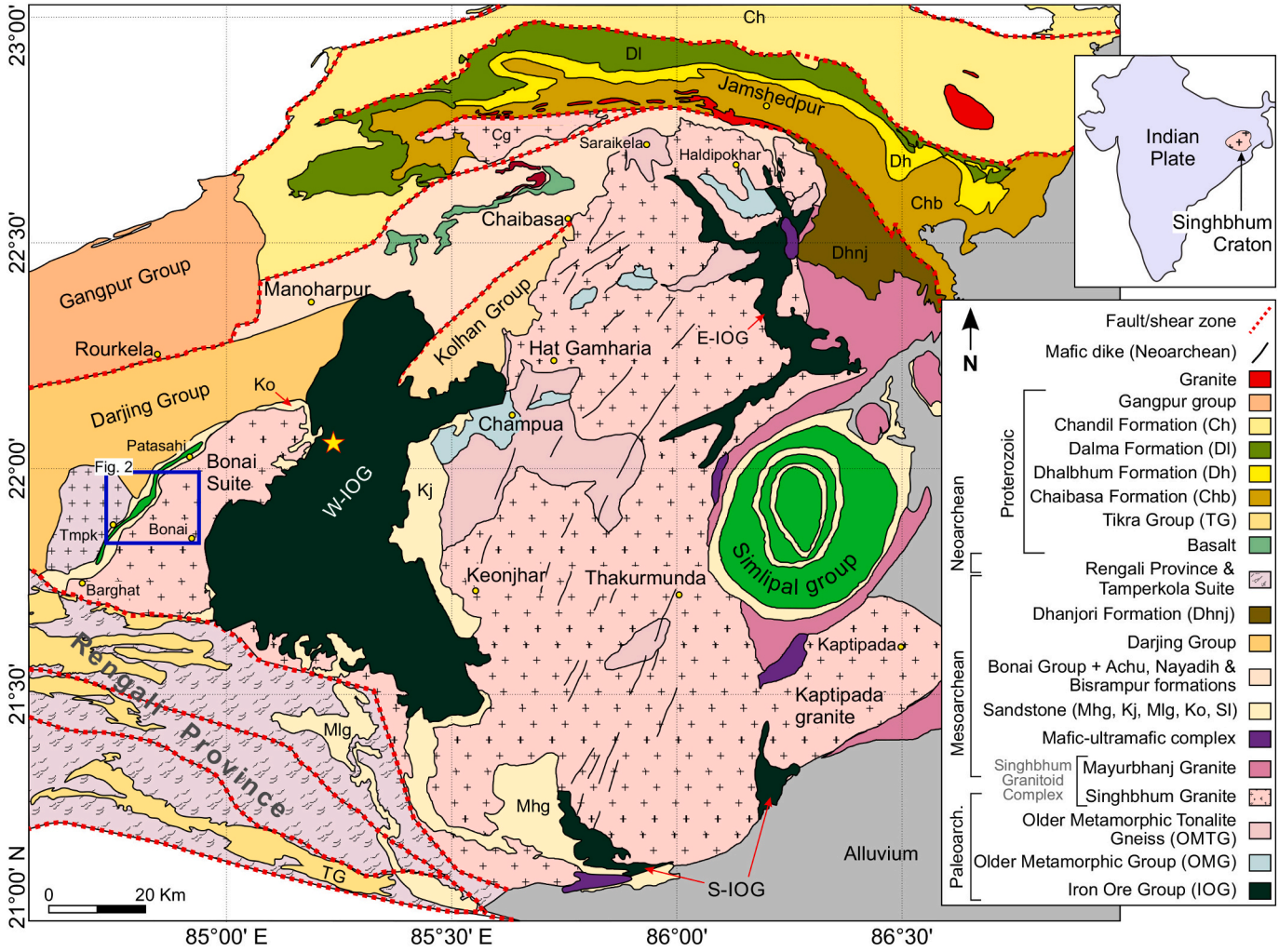

Fig. 1. Geological map of the Singhbhum Craton, modified from Olierook et al. (2019) and Hofmann et al. (2022), showing main lithologies and their stratigraphic position, major faults, and the study area. The yellow star indicates the location of lower lava flows of the W-IOG studied by Wright and Basu (2024). Tmpk—Tamperkola Suite, Cg—Chakradharpur granite, Mhg—Mahagiri quartzite, Kj—Keonjhar quartzite, Mlg—Malaygiri quartzite, Ko—Koira quartzite, Sl—Simlipal Group. (For interpretation of the references to colour in this figure legend, the reader is referred to the web version of this article.)

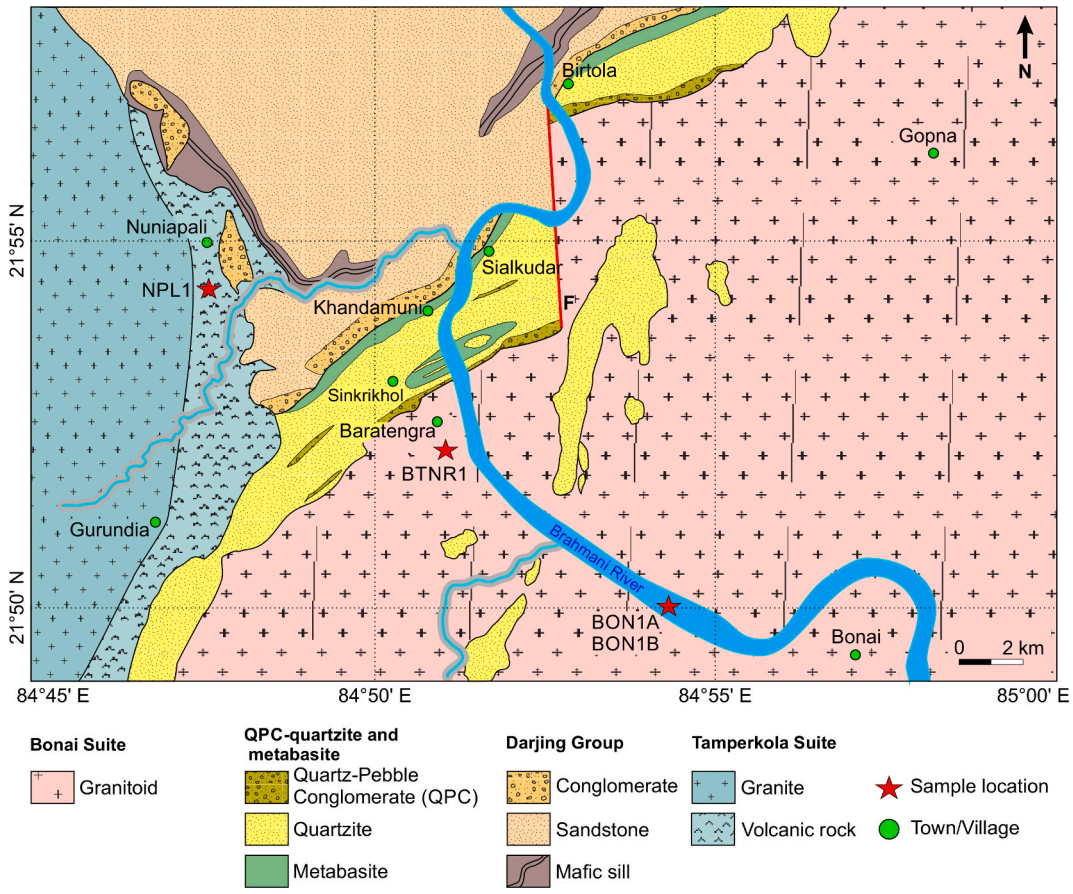

Fig. 2. Geological map of the study area showing studied rock units and their contacts, and sample locations (red stars), modified from Kumar et al. (2012), Jana et al. (2016), Jana and Sinha (2021), and Alam et al. (2022). (For interpretation of the references to colour in this figure legend, the reader is referred to the web version of this article.)

2. Geological setting

The Singhbhum Craton comprises an area of ~50,000 km^2 in the eastern part of the Indian Plate. Figure 1 presents the Archean–Proterozoic rock record of the Singhbhum Craton. The Iron Ore groups (IOG) consist of weakly to moderately deformed successions of ultramafic to felsic lavas, clastic sedimentary rocks, and banded iron formations, which are exposed along three belts (eastern, western, and southern) encircling the TTG-granite core of the craton (Mazumder et al., 2012; Mukhopadhyay et al., 2012; Mazumder et al., 2019; Mazumder and Chaudhuri, 2021; Mazumder et al., 2022). Depositional ages of the IOG successions range from ca. 3500 to ca. 3300 Ma (Mukhopadhyay et al., 2008; Sreenivas et al., 2019; Jodder et al., 2021; Hofmann et al., 2022; Jodder et al., 2023; Wright and Basu, 2024). The Older Metamorphic Group (OMG) and Older Metamorphic Tonalite Gneiss (OMTG) consist of strongly deformed supracrustal rocks including quartzite, metapelite, amphibolite, and calc-silicate (OMG), and TTG gneiss and smaller granitic counterparts (OMTG), which are mostly formed at ca. 3400 Ma (Mishra et al., 1999; Acharyya et al., 2010; Nelson et al., 2014; Upadhyay et al., 2014; Hofmann and Mazumder, 2015; Dey et al., 2017; Chaudhuri et al., 2018; Mitra et al., 2019; Hofmann et al., 2022). The Singhbhum Granitoid Complex (SGC) is a multiphase granitoid that dominates the central part of the craton and consist of weakly deformed to undeformed TTG granitoids in the early phases emplaced between ca. 3300 to ca. 3100 Ma and transitional to more K-rich granites during the later phases at ca. 3100 Ma to ca. 3050 Ma (Nelson et al., 2014; Upadhyay et al., 2014; Chaudhuri et al., 2018; Dey et al., 2019; Mitra et al., 2019; Olierook et al., 2019; Pandey et al., 2019; Zoleikhaei et al., 2023). Several other plutonic rocks including the Bonai, Kaptipada, and Chakradharpur granitoids occur toward the margins of the craton and are also attributed to the SGC magmatism (Fig. 1; Vohra et al., 1991; Saha, 1994; Chakraborty et al., 2019; Ghose and Saha, 2019; Asokan et al., 2021). However, their temporal, compositional, and geographical relationships with the central body of the SGC have remained poorly resolved (Hofmann et al., 2022). The younger Meso-Neoarchean plutonic-volcanic suites including Tamperkola, Budhapal, Kalinganagar, and Pallahara granites intrude into the weakly to moderately deformed Mesoarchean successions in the western and southwestern margins of the carton (Sengupta et al., 1991; Bandyopadhyay et al., 2001; Bose et al., 2016; Topno et al., 2018).

The geological evolution of the rock units in the western part of the Singhbhum craton is poorly resolved (Fig. 2). Although several studies have attempted to determine the emplacement ages of the Bonai and Tamperkola suits, the reported ages are either associated with large uncertainties (whole rock Sm—Nd ages; Sengupta et al., 1991) or represent upper intercept ages from highly discordant and scattered data (zircon U—Pb ages; Sengupta et al., 1996; Bandyopadhyay et al., 2001; Chakraborty et al., 2019; Asokan et al., 2021). Furthermore, the absence of isotopic data hampered evaluation of magma genesis for these plutons. Mitra et al. (2022) reported a reasonably precise age (3368 ± 7 Ma) and Hf isotope ($\varepsilon Hf_{(t)} = +2.3$ to $+4.3$) data from concordant zircon grains in a migmatitic gneiss enclave in the Bonai Suite, but such data are not available for the host rock and the microgranular mafic enclaves.

2.1. Sample description and petrography

2.1.1. Bonai Suite

The Bonai Suite has a heterogenous composition comprising an

equigranular feldspathic augen gneiss (Fig. 3A and B) and a deformed equigranular to porphyritic granite (Fig. 3F and G) ranging in composition from TTG to granite. Both rock types exhibit one prominent foliation, which in the augen gneiss is tightly folded and is parallel to the gneissosity. Enclaves of variable origins and sizes, including mafic orthogneiss and migmatitic melanosome ranging in size from a few centimeters to tens of meters, form the third component of this pluton (Fig. 3C–E). Mafic schlieren bands are commonly observed within this rock in the outcrop. The Bonai Suite is bounded to the east, north, and west by quartzite with conglomerate lenses, and mafic volcanic rocks (Figs. 1 and 2). These surrounding rocks are commonly assigned to the Western Iron Ore Group (W-IOG) (e.g., Sengupta et al., 1991; Sengupta et al., 1996; Kumar et al., 2009). However, in the east the Bonai Suite intrudes into the mafic volcanic rocks, whereas in the north and west quartzite and conglomerate sequences unconformably overlie the suite (Sengupta et al., 1991; Kumar et al., 2009). In the south, the Bonai Suite is in fault contact with the Meso-Neoarchean Rengali Province gneisses and quartzites (Fig. 1). We sampled an equigranular augen gneiss (BON1A) and a mafic enclave (BON1B) from the bed of the Brahmani River near the village of Narendra (N21°50′01.7″, E84°54′19.2″), and a porphyritic granite (BTNR1) near Baratangarha village (N21°52′09.2″, E84°51′02.7″; Fig. 2).

The equigranular augen gneiss (BON1A) is dominantly composed of plagioclase and quartz with minor K-feldspar and altered biotite and muscovite (Fig. 3A and B). The feldspar grains exhibit deformation lamellae, grain boundary recrystallization, and are partially altered to sericite, chlorite, minor epidote, and rarely to muscovite. The quartz grains have wavy extinction with deformed boundaries and form ribbon structures (Fig. 3B). Microscale bands of chlorite, mica, and epidote form along the foliation plane swerving and cutting across the original

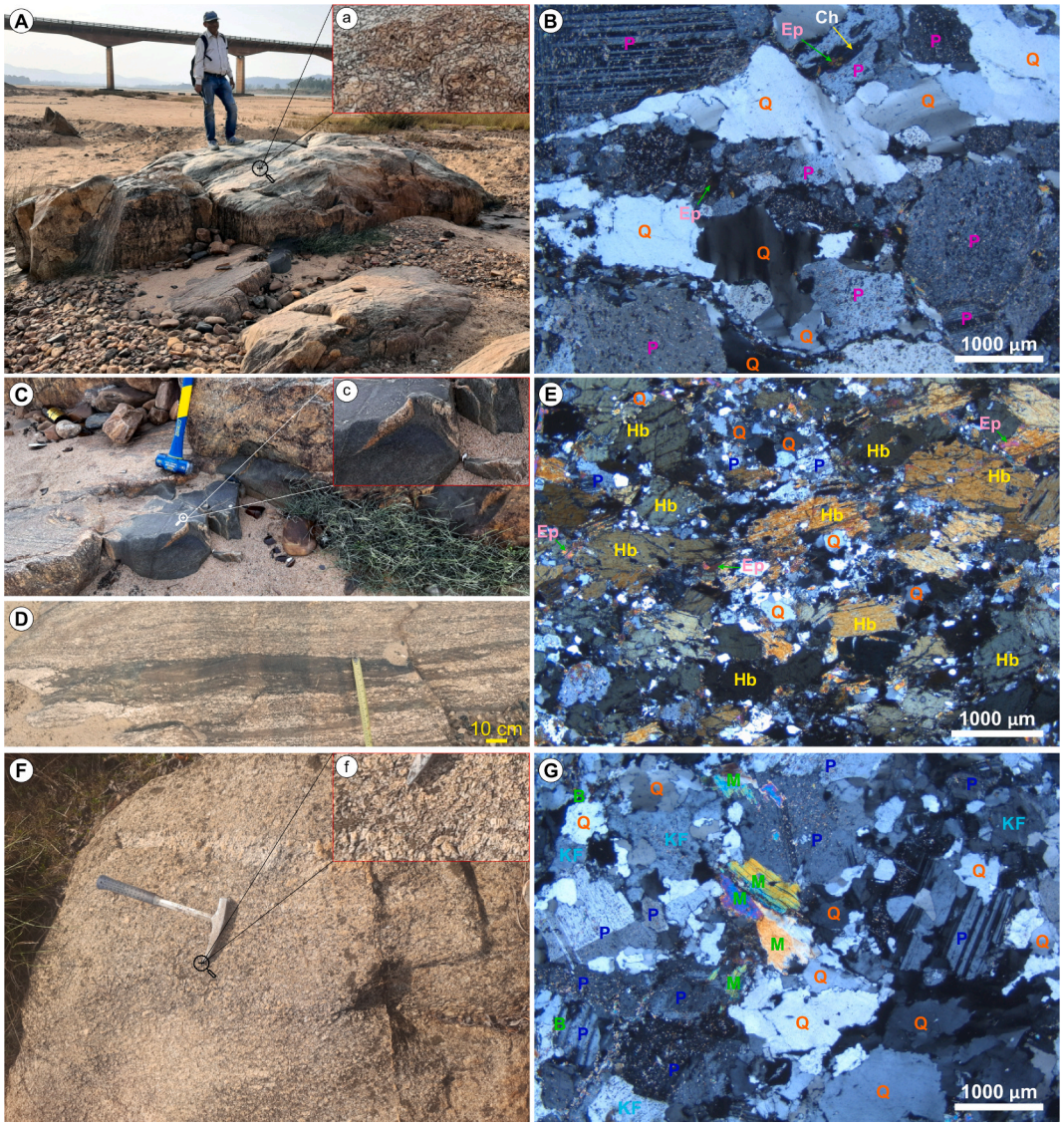

Fig. 3. Field photographs and polarized light photomicrographs from the three rock types of the Bonai Suite. A and B) Bonai equigranular TTG gneiss and an enclosed mafic enclave. Inset (a) shows magnified view of the texture of the rock. The photomicrograph highlights the dominance of plagioclase over K-feldspar, alteration of plagioclase crystals, and the deformed texture of the rock with quartz crystals forming ribbon structure. C—E) Mafic enclave in the Bonai equigranular TTG gneiss as rounded globules (C) and as schlieren bands (D). The magnified view in inset (c) shows felsic veins crosscutting the mafic enclave. The photomicrograph shows the dominance of hornblende with less frequent plagioclase and minor secondary quartz. Hornblende crystals show incipient alteration to chlorite and epidote. F and G) Bonai porphyritic granite, with a magnified view of the rock texture in inset (e). The photomicrograph shows the higher K-feldspar content and less deformed nature of this rock compared to the Bonai equigranular TTG gneiss. Deformation evidence include subgrain deformation, grain boundary recrystallization, and replacement of K-feldspar by secondary muscovite. P—plagioclase, Q—quartz, Ep—epidote, Ch—chlorite, Hb—hornblende, KF—K-feldspar, M—muscovite, and B—biotite.

quartz-albite association suggesting they are secondary in origin (Fig. 3A and B). The secondary mineral assemblages (i.e., sericite, mica, chlorite, and epidote) and deformational structures (i.e., stretched quartz crystals) indicate that the rock underwent greenschist facies of metamorphism. The prevalence of plagioclase over K-feldspar points to a tonalite-trondhjemite-granodioritic composition for this pluton, which is also indicated by previous whole-rock geochemical data (supplementary Fig. S1; Sengupta et al., 1991). Hereafter we refer to this pluton as Bonai TTG gneiss.

The sample from the mafic enclave (BON1B) comprises abundant hornblende, and less frequent plagioclase and quartz with minor apatite (Fig. 3C–E). The hornblende crystals are only weakly oriented and show minor alteration to chlorite and epidote (Fig. 3E). Occasionally, thin (≤1 cm thick) felsic veins, similar in texture and composition to host TTG gneiss, cut across the enclaves (Fig. 3C). The secondary mineral assemblage and minimal deformation points to a sub-greenschist metamorphic facies, which is comparable to the degree of metamorphism in the host rocks. Given the prevalence of hornblende and plagioclase and the metamorphic grade, this rock is classified as an amphibolite.

The porphyritic granite sample of the Bonai Suite (BTNR1) consist of plagioclase, quartz, K-feldspar, and mica in the order of abundance (Fig. 3F and G). Feldspar crystals form the phenocrysts and are mostly well-preserved with some grains showing incipient evidence of sericitization. Quartz crystals have wavy extinction with grain boundary migration and bulging recrystallization (Fig. 3G). Muscovite and biotite crystals are well-preserved and are only sporadically compressed. Published whole-rock major element data demonstrate a high potassium (K_2O = 4.17 wt%) character for this granite (Fig. S1; Sengupta et al., 1991). This sample is classified as a granite and hereafter is referred to as the Bonai porphyritic granite.

2.1.2. Tamperkola Suite

The Tamperkola granite-felsic volcanic Suite includes a dominant pink colored, fine-grained equigranular to porphyritic granite and a less common dark colored, dominantly porphyritic acid volcanic body. The acid volcanic rocks occur as an elongated bow-shaped body along the eastern margin of the granite (Fig. 2). The Tamperkola Suite occurs to the west of the Bonai Suite and its granite body intrudes into the quartzites covering the Bonai Suite and the Darjing Group supracrustal rocks that cover these quartzites (Figs. 1 and 2). The suite is largely undeformed, but near the margins it displays a crude foliation defined by flattening of quartz and biotite that swerves around the feldspar phenocrysts. One sample from the felsic volcanic body (NPL1) was collected near Kantapali village (N21°54′21.2″, E84°47′36.0″; Fig. 2). Under the microscope, this sample exhibits porphyritic texture with K-feldspar, microcline, and subordinate plagioclase phenocrysts, ranging in size from 0.5 to 1.5 cm, in a fine-grained groundmass (30–50 μm) composed of quartz and feldspar, with minor muscovite and biotite (Fig. 4). The feldspar phenocrysts are equidimensional or rarely elongated with marginal recrystallization, which in more deformed cases develop into strain shadow. The quartz and feldspar crystals in the groundmass show sutured contacts (Fig. 4B). Muscovite grains form within or along grain boundaries of the K-feldspars suggesting that they are secondary in origin (Fig. 4B). Given the aphanitic texture of the groundmass and the dominance of felsic minerals (i.e., quartz and feldspar), and a rhyolitic composition based on whole-rock major elements data (Fig. S1; Bandyopadhyay et al., 2001), this sample is classified as a porphyritic rhyolite. Published whole-rock major element data indicate a high-K (K_2O = 4.91–5.25 wt%) nature for the Tamperkola rhyolite and granite (Fig. S1; Bandyopadhyay et al., 2001; Alam et al., 2022).

3. Analytical methods

3.1. Zircon U-Pb-Hf analysis

Approximately 1 kg of each of the samples was crushed using a jaw crusher and a tungsten carbide ring mill. The pulverized material was sieved with a metal sieve with 355 μm apertures, and the fraction below 355 μm was selected for further mineral processing. Heavy minerals concentration from the selected material was performed by gravity separation using Wilfley-Holman water table, followed by magnetic separation using Frantz magnetic separator set at 0.5 A, and gravity separation using tetrabromoethane (2.96 g/cm^3). At least 100 zircon grains were hand-picked and mounted on glass slides. These grains were then set into epoxy resin blocks of 2.5 cm diameter and polished to expose their middle sections. For selecting analytical spots cathodoluminescence (CL) images of the zircon grains were captured using a Phillips FEI XL30 environmental scanning electron microscope equipped with a Gatan PanaCL detector housed at the University of Melbourne, Australia. The analytical spots are commonly placed on the grains mantles away from inherited cores. However, in grains with amorphous internal structure the central part of the grains is targeted.

Between 35 and 40 zircon grains from each sample were selected for U—Pb age and Hf isotope analyses. The analyses were conducted via split-stream Laser Ablation-Inductively Coupled Plasma-Mass Spectrometry during which a RESolution 193 nm laser was coupled with a Thermo Fisher iCAP Tetra Quadrupole ICP-MS for measuring U and Pb isotopes, and a Thermo Fisher Neptune Multicollector ICP-MS for measuring Lu and Hf isotopes. The analysis involved 30 s of blank measurement followed by 60 s ablation using a laser beam of 35 μm diameter, 4 J/cm^2 on sample fluence, and a repetition rate of 8 Hz. The reference zircons OG1 (Stern et al., 2009) and MudTank (Woodhead and Hergt, 2005) were analyzed as the primary reference materials for calibrating the U—Pb and Lu—Hf measurements, respectively. The QGNG

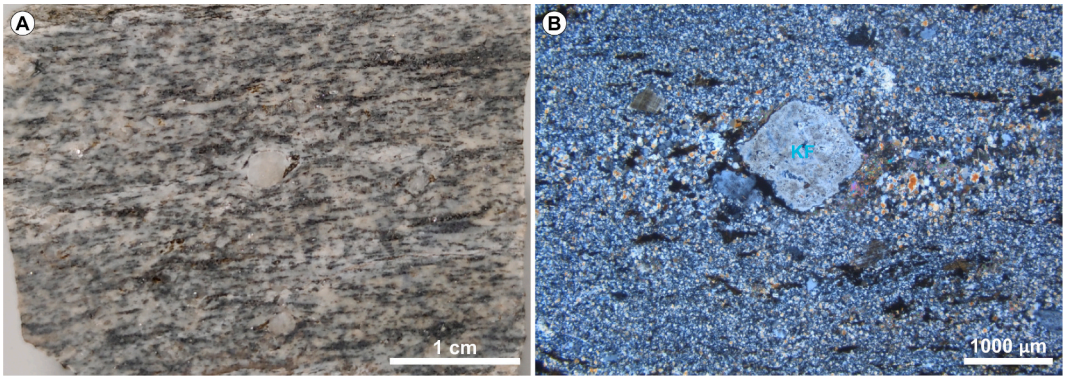

Fig. 4. Hand specimen photo (A) and polarized light photomicrograph (B) from the Tamperkola rhyolite. The groundmass comprises recrystallized quartz, feldspar, and sericite. The phenocrysts are dominantly K-feldspar with minor plagioclase.

(Black et al., 2003), 91500 (Wiedenbeck et al., 1995), GJ1 (Jackson et al., 2004), and Plešovice (Sláma et al., 2008) zircons were analyzed as secondary reference materials for checking the quality and accuracy of the measurements. The collected raw data for U—Pb isotopes and Lu—Hf isotopes were reduced using the inbuilt *U—Pb Geochronology* and *Hf Isotopes* data reduction schemes in Iolite 4 software (Paton et al., 2011). The Lu—Hf measurements were corrected for mass interference of ^{176}Yb and ^{176}Lu on ^{176}Hf using the peak-striping method (e.g., Woodhead et al., 2004; Fisher et al., 2011; Fisher et al., 2014; Spencer et al., 2020). The amount of ^{176}Yb and ^{176}Lu were calculated by measuring interference-free isotopes (i.e., ^{171}Yb, ^{173}Yb, and ^{175}Lu) and using the accepted natural ratios (^{176}Yb/^{173}Yb = 0.796218, ^{173}Yb/^{171}Yb = 1.132685, and ^{176}Lu/^{175}Lu = 0.02656; Chu et al., 2002). In these calculations mass bias of Yb (βYb) and Hf (βHf) were calculated using measured ^{173}Yb/^{171}Yb and ^{179}Hf/^{177}Hf ratios, respectively, and βLu was considered to be equal to βYb (Woodhead et al., 2004; Fisher et al., 2011). The applied mass interference correction removes most of the covariation between ^{176}Lu (^{176}Yb) and ^{176}Hf, and the remaining covariation between these isotopes in the analyzed Archean samples and OG1 reference material resembles an isochron relationship between the radioactive (^{176}Lu) and radiogenic (^{176}Hf) isotopes (cf. Maltese et al., 2021; Zoleikhaei et al., 2023). The measured weighted mean ages and ^{176}Hf/^{177}Hf ratios for the reference material analyzed in this study overlap within uncertainties with the recommended values (supplementary files A and B). The concentrations of the trace elements ^{178}Hf, ^{173}Yb and ^{175}Lu were calculated from the same data that were collected for Lu—Hf isotopic analysis. The data were reduced using the *Trace Element* data reduction scheme in Iolite 4 with zircon 91500 used as the primary reference material. Data tables for zircon U—Pb, Lu—Hf, and trace elements are reported in supplementary files A and B.

All presented age values are ^{207}Pb/^{206}Pb ages unless specified otherwise, and the reported uncertainties for individual ages are propagated 2 se. The uncertainty calculations for the weighted mean ages follows the procedure described in Horstwood et al. (2016), which

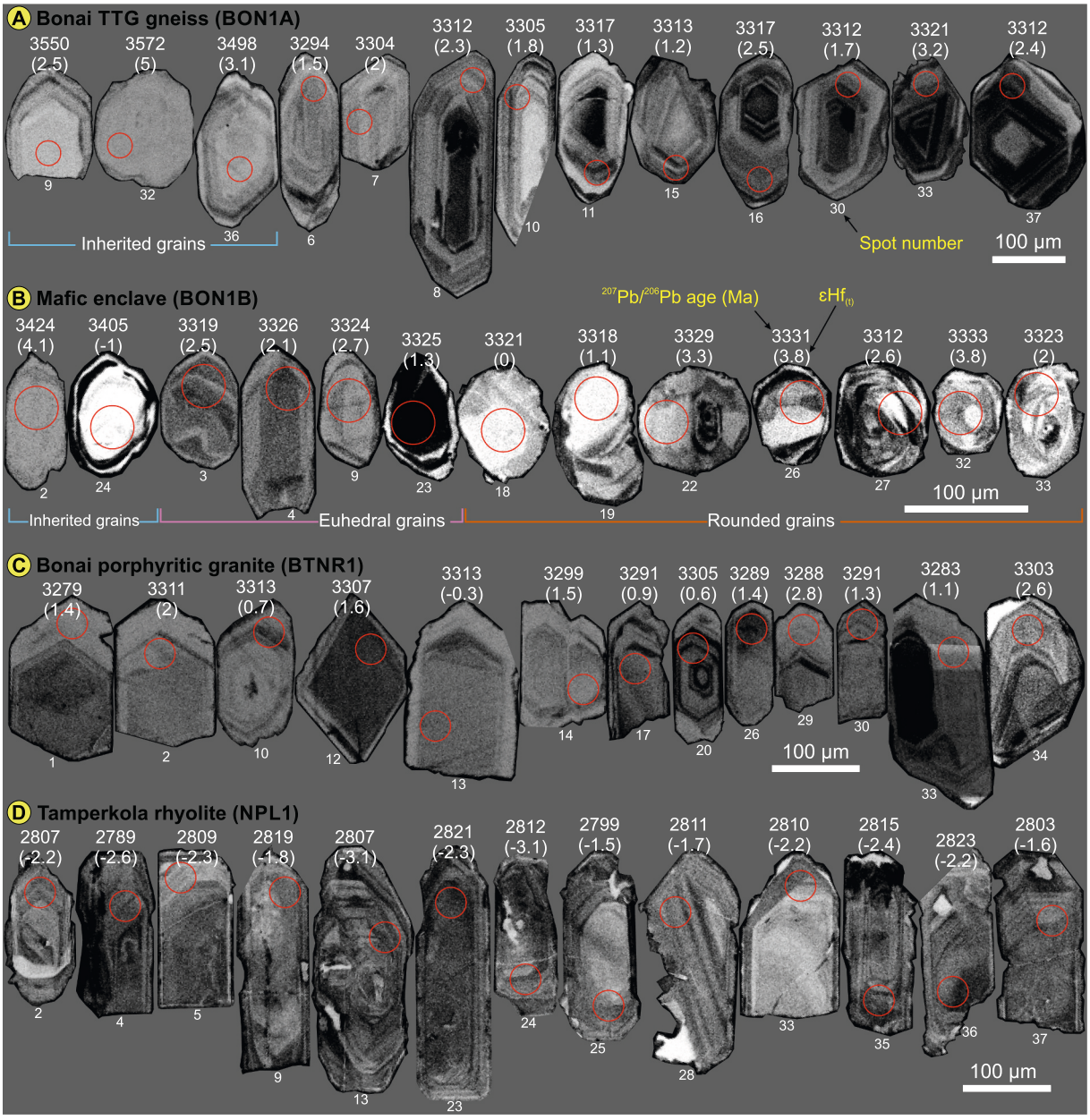

Fig. 5. Example cathodoluminescence (CL) images from the analyzed zircon grains from the Bonai TTG gneiss (A), mafic enclave in Bonai TTG gneiss (B), Bonai porphyritic granite (C), and Tamperkola rhyolite (D).

includes quadratic addition of systematic uncertainties to the measurement uncertainties after defining the weighted mean ages. The considered sources of systematic uncertainty include ratio uncertainty of the primary reference material, excess variance of the secondary reference material, and decay constant uncertainties, which equal to 0.23 % (2 se) for $^{206}Pb/^{238}U$ and 0.25 % (2 se) for $^{207}Pb/^{206}Pb$.

4. Results

The analyzed zircon grains include concordant (< ±3 % discordant, discordance = (1 - $^{206}Pb/^{238}U$ age ÷ $^{207}Pb/^{206}Pb$ age) × 100) and discordant (> ±3 % discordant) ages. The weighted mean ages are calculated using only the concordant ages. The presented $^{176}Hf/^{177}Hf_{(t)}$ and $\varepsilon Hf_{(t)}$ values for concordant grains are based on their individual measured ages, whereas for the discordant grains the weighted mean age of the concordant grains from the same group is used, and if this age is not available or considered unreliable, the upper intercept age of their discordia is used.

4.1. Bonai Suite

4.1.1. Bonai TTG gneiss (BON1A)

Zircon grains in the Bonai TTG gneiss have elongated to stubby prismatic shapes and range in size from 50 μm to 350 μm (Fig. 5A). In the CL images most grains have well-preserved oscillatory zoning. However, a minor fraction of grains are amorphous in the center and only show faint zoning toward the edges (Fig. 5A). Occasionally, some grains might include inherited cores with marginal dissolution bays. The analyzed zircon grains ($n = 40$) from this sample have variable and typically high U (55–1730 ppm, average 489 ppm) and Th (19–986 ppm, average 170 ppm) contents. Their Th/U ratios are variable (0.04 to 1.64) but mostly (85 %) > 0.1 (Fig. 6A).

The zircon U—Pb ages of the Bonai TTG gneiss include two groups of concordat ages with both having associated discordant grains (Fig. 6A). The first and largest group of ages is from the grains with relatively well-preserved internal zoning (Fig. 6A). The concordant (discordance % = −0.3 to 2.8) ages in this group comprises 26 grains with ages between 3333 Ma to 3301 Ma and $^{176}Hf/^{177}Hf_{(t)}$ between 0.280634 to 0.280757

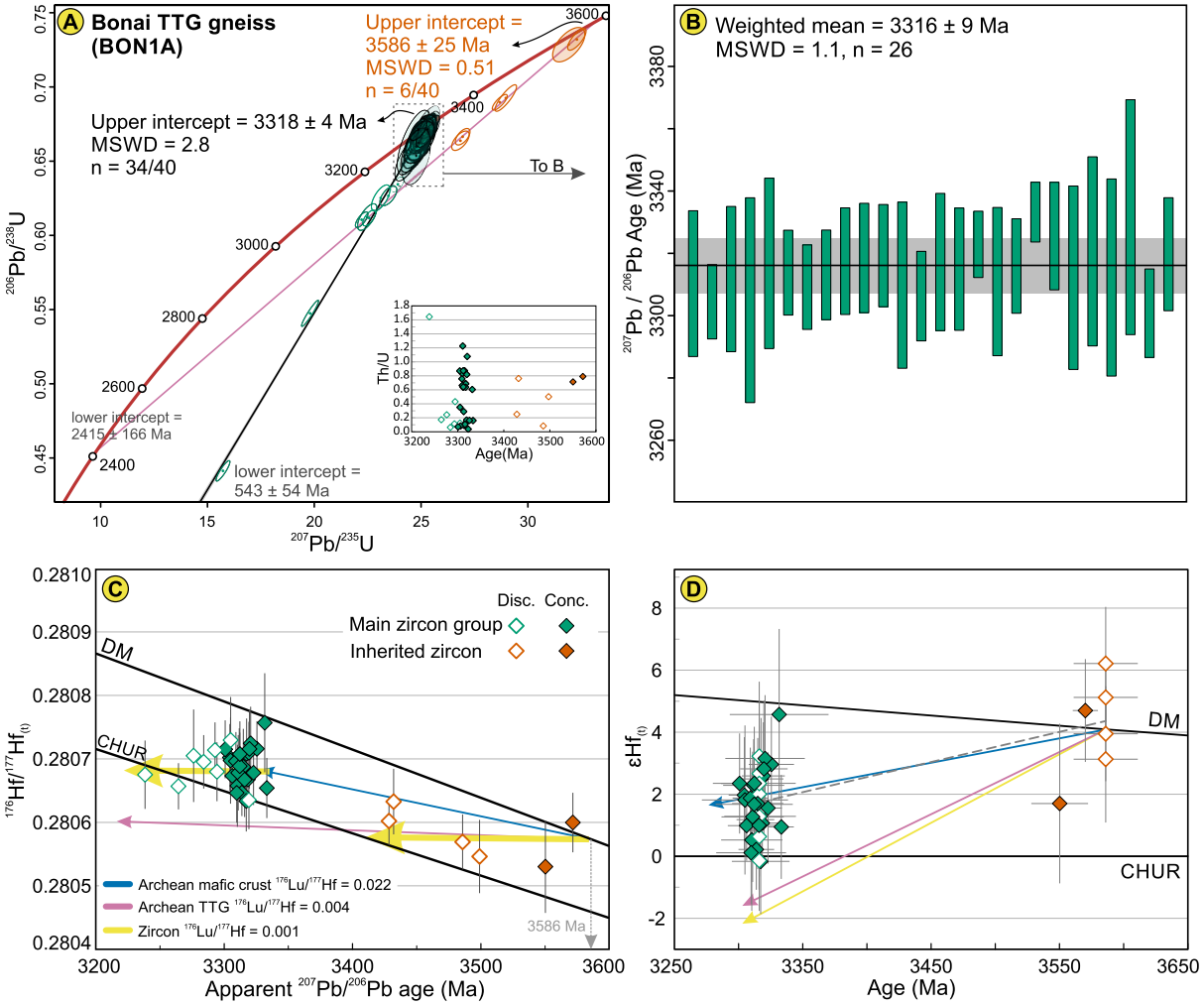

Fig. 6. (A) U—Pb concordia and Th/U scatter plot for the zircon grains analyzed from the Bonai TTG gneiss. B) Weighted mean plot for the concordant zircon ages in the primary age group. C) Plot of initial $^{176}Hf/^{177}Hf$ ratios versus measured ages of the zircon grains demonstrates that the igneous and inherited zircon groups have distinct Hf isotope composition. However, the discordant zircon grains in each group exhibit Hf isotope compositions similar to those of the associated concordant grains and follow a trajectory with $^{176}Lu/^{177}Hf = 0.001$, typical of zircon. D) Plot of $\varepsilon Hf_{(t)}$ versus age showing that the $\varepsilon Hf_{(t)}$ values of the igneous zircon grains are dominantly suprachondritic and the $\varepsilon Hf_{(t)}$ values of the inherited zircon grains plot on the depleted mantle array. The slope of regression line (0.009) between the igneous and inherited zircon grains in this sample (grey dashed line) corresponds to a $^{176}Lu/^{177}Hf = 0.02$, which is similar to that of the Archean mafic crust with $^{176}Lu/^{177}Hf = 0.022$ (dark blue arrow; Amelin et al., 1999). The $\varepsilon Hf_{(t)}$ values are calculated using ^{176}Lu decay constant of Söderlund et al. (2004). DM: depleted mantle (Vervoort and Blichert-Toft, 1999), CHUR: chondrite uniform reservoir (Bouvier et al., 2008), Archean TTG $^{176}Lu/^{177}Hf$ is from Guitreau et al. (2012). (For interpretation of the references to colour in this figure legend, the reader is referred to the web version of this article.)

(Fig. 6A and C). These grains yield a weighted mean age of 3316 ± 9 Ma (Fig. 6B). The eight discordant (discordance % = 4.6 to 27) grains associated with this group have ages between 3319 Ma to 3238 Ma and follow a congruent discordia pattern away from the concordant ages (Fig. 6A). The Hf isotope composition of these grains, $^{176}Hf/^{177}Hf_{(3316\ Ma)}$ between 0.280635 to 0.280730, are also similar to those of the concordant grains (Fig. 6C). A discordia line regressed thought all grains in this group provide upper and lower intercept ages respectively at

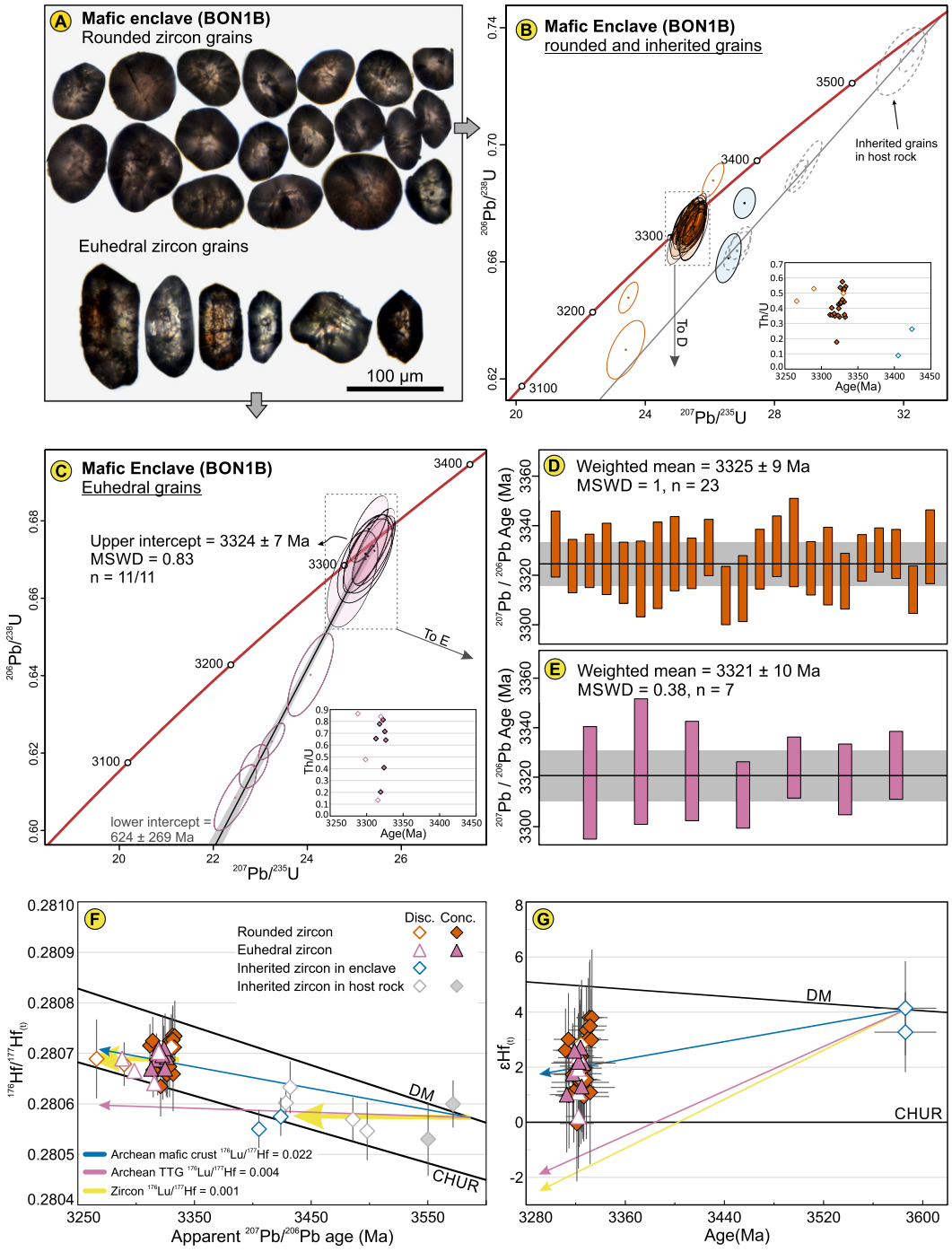

Fig. 7. (A) Transmitted light images of the zircon grains from the mafic enclave with different rounded and euhedral morphologies. B) Zircon U—Pb concordia and Th/U scatter plot for the rounded and inherited zircon grains. The grains with empty error ellipses are not used in calculating the weighted mean age. The two older and discordant zircon grains with pale blue fill color mainly follow the discordia pattern of the inherited zircon grains in the host Bonai TTG gneiss (grains with dashed grey outlines). C) Zircon U—Pb concordia and Th/U scatter plots for the euhedral zircon grains. D and E) Weighted mean age plots for the rounded and euhedral zircon grains with concordant ages. F) Initial $^{176}Hf/^{177}Hf$ ratio versus measured age plot for the rounded and euhedral grains. The rounded and euhedral grains exhibit similar Hf isotope compositions, and their associated discordant grains follow the evolutionary trend of zircon with $^{176}Lu/^{177}Hf = 0.001$. The two older discordant grains with blue outlines exhibit Hf isotope compositions similar to the inherited zircon grains in the host Bonai TTG gneiss (grains with grey fills and outlines). G) Plot of $\varepsilon Hf_{(t)}$ versus age indicates similar and suprachondritic Hf isotope signatures for both the rounded and euhedral zircon grains, and mantle-like $\varepsilon Hf_{(3586\ Ma)}$ values for the two older, discordant zircon grains. The time-integrated Hf isotope composition of the rounded and euhedral zircon groups plot on the evolution array of the older zircon grains given a $^{176}Lu/^{177}Hf$ ratio of 0.022, equal to that of the Archean mafic crust (dark blue arrow). (For interpretation of the references to colour in this figure legend, the reader is referred to the web version of this article.)

3318 ± 4 Ma and 543 ± 54 Ma (Fig. 6A). This upper intercept age is within uncertainties of the weighted mean age of the concordant grains. Thus, given the CL features of this group of grains, we consider the weighted mean age of 3316 ± 9 Ma to represent the crystallization age of the Bonai TTG gneiss.

The second group of ages in this sample is from zircon grains with amorphous or poorly-preserved internal zoning (Figs. 5A and 6A). This group comprises two concordant (discordance % = 0.6 to 0.9) ages at 3572 Ma and 3550 Ma, with $^{176}Hf/^{177}Hf_{(t)}$ values of 0.280600 and 0.280530. These grains yield a weighted mean age of 3568 ± 12 Ma with an MSWD of 3.1. The remaining four discordant (discordance % = 3 to 4.4) grains in this group have ages between 3498 Ma to 3428 Ma and follow a congruent discordia pattern away from the concordant grains (Fig. 6A). The $^{176}Hf/^{177}Hf_{(3586\ Ma)}$ values (0.280546 to 0.280633) of these grains are similar to those of the concordant grains (Fig. 6C). The U—Pb discordia regressed through all grains in this group yields upper and lower intercept ages respectively at 3586 ± 25 Ma and 2415 ± 166 Ma. Although overlapping within uncertainties, the weighted mean age of the two concordant grains is ca. 20 Myr younger than the upper intercept age of the discordia, is derived from only two ages, and has a high MSWD. Thus, the upper intercept age represents the best estimation on the crystallization age of these grains. This age closely corresponds to the T_{DM2} age of the primary zircon group discussed below, which suggests inherited source for the old grains.

The $\varepsilon Hf_{(t)}$ values range between −0.2 to +4.6 for the primary zircon group, and between +1.7 to +6.2 for the older age group (Fig. 6D). The time-integrated evolutionary trend of Hf isotopes between the inherited and igneous zircon grain yields a $^{176}Lu/^{177}Hf$ ratio of 0.02 (Fig. 6D), which is close to that of the Archean mafic crust ($^{176}Lu/^{176}Hf = 0.022$; Amelin et al., 1999). Two-stage model ages (i.e., the age of extraction from Depleted Mantle; T_{DM2}) calculated for the primary zircon group, using $^{176}Lu/^{177}Hf = 0.022$ in the calculations for the second stage, yield ages between 3789 Ma to 3365 Ma (average = 3617 Ma).

4.1.2. Mafic enclave in the Bonai TTG gneiss (BON1B)

Zircon grains from the mafic enclave have reddish pink color and range in size from 50 μm to 150 μm with bimodal shapes (Fig. 7B). The majority of the grains are rounded with high luster, and a minor portion of grains have euhedral prismatic shape (Fig. 7A). In the CL images, both groups preserve faint evidence of growth zoning and rarely include overgrowth rims or inherited cores (Fig. 5B). The analyzed zircon grains contain variable and dominantly high U (123–1161 ppm, average 334 ppm) and Th (67–305 ppm, average 131 ppm) contents. Their Th/U ratios range from 0.09 to 0.87 with the majority (97 %) of grains having Th/U > 0.1 (Fig. 7B).

Most of the analyzed zircon grains from the group with rounded morphologies yield concordant (discordance % = −0.3 to 0.9) ages, making a single population with ages between 3333 Ma to 3312 Ma and similar $^{176}Hf/^{177}Hf_{(t)}$ values between 0.280635 to 0.280736 (Fig. 7B). These grains define a weighted mean age of 3325 ± 9 Ma (Fig. 7D). The four discordant (discordance % = −1.3 to 4.3) grains in this group do not make a clear discordia array, but three grains show similar age (3330 Ma to 3266 Ma) and $^{176}Hf/^{177}Hf_{(3325\ Ma)}$ values (0.280679 to 0.280713) to those observed in the concordant zircon grains (Fig. 7F). The $\varepsilon Hf_{(t)}$ values of the rounded zircon grains range from 0 to +3.8 (Fig. 7G). The T_{DM2} ages for these grains, calculated using mafic crust $^{176}Lu/^{177}Hf$ ratio of 0.022, range between 3781 Ma to 3436 Ma (average = 3588 Ma).

The analyzed zircon grains with euhedral morphologies show age and Hf isotopes similar to those of the rounded zircon grains. The majority of these grains (7/12) show concordant (discordance % = −0.6 to 1) ages, making a single group with ages between 3326 Ma to 3313 Ma (Fig. 7C) and similar $^{176}Hf/^{177}Hf_{(t)}$ values between 0.280699 to 0.280710 (Fig. 7F). These grains yield a weighted mean age of 3321 ± 10 Ma (Fig. 7E). The four discordant (discordance % = 4 to 6.9) grains associated with this group yield ages between 3319 Ma to 3288 Ma and follow a discordia pattern deviating from the concordant ages. The $^{176}Hf/^{177}Hf_{(3321\ Ma)}$ values in these grains range between 0.280641 to 0.280703, which is also similar to that of concordant grains (Fig. 7F). A discordia line regressed through the concordant and discordant ages in this group defines upper and lower intercept ages respectively at 3324 ± 7 Ma and 624 ± 269 Ma (Fig. 7C). The $\varepsilon Hf_{(t)}$ values of the euhedral grains range from +0.2 to +2.7(Fig. 7G). The T_{DM2} ages for these grains, calculated using mafic crust $^{176}Lu/^{177}Hf$ ratio of 0.022, range between 3752 Ma to 3530 Ma (average = 3614 Ma).

The remaining two grains in this sample, one with rounded and one with euhedral morphology, are 1.8 % and 4.5 % discordant (Fig. 7B). These grains do not make a clear discordia array, but mostly follow the discordia array defined by the inherited zircon grains in the host Bonai TTG gneiss with ca. 3586 Ma upper intercept age (Fig. 7B). The $^{176}Hf/^{177}Hf_{(3586\ Ma)}$ values of these two grains, at 0.280550 and 0.280575, is also similar to those from the inherited zircon grains in the host rock (Fig. 7F).

Despite the similar age and Hf isotope compositions for the rounded and euhedral zircon grains, they have distinct trace elements compositions. The rounded zircon grains show lower Yb (59–142 ppm), Lu (13–29 ppm), and Hf (7995–11288 ppm) contents compared to the associated euhedral grains with Yb (439–797 ppm), Lu (74–135 ppm), and Hf (10654–18954 ppm) (Fig. 8). The higher Lu, Yb, and Hf contents in the euhedral zircon grains resemble the values observed in the zircon grains from the host Bonai TTG gneiss (Fig. 8). Given the complexities in morphology and trace element compositions of the zircon grains, interpretations of crystallization age for this sample are given in Section 5.1.2.

4.1.3. Bonai porphyritic granite (BTNR1)

Zircon grains in the Bonai porphyritic granite are transparent and euhedral pink grains with elongated to stubby prismatic shapes, and range in size from 50 μm to 300 μm. In the CL images, the majority of the grains preserve oscillatory growth zoning (Fig. 5C). The analyzed zircon grains (n = 39) have variable and generally high U (66–1213 ppm, average 398 ppm) and Th (20–1289 ppm, average 215 ppm) contents, and their Th/U ratios range from 0.12 to 1.58 (Fig. 9A).

Most of the zircon grains from this sample are concordant (discordance % = −0.3 to 2.4), making a single group with ages between 3313 Ma to 3278 Ma (Fig. 9A) and similar $^{176}Hf/^{177}Hf_{(t)}$ values between 0.280633 to 0.280747 (Fig. 9C). These ages define a weighted mean age at 3299 ± 9 Ma (Fig. 9B). The discordant ages include seven grains (discordance % = 3.4 to 18.6) with ages between 3313 Ma to 3270 Ma. Most of these ages follow a discordia pattern away from the main concordant group (Fig. 9A) and their $^{176}Hf/^{177}Hf_{(3299\ Ma)}$ values (0.280603 to 0.280746) are also similar to those of the concordant ages (Fig. 9C). A discordia line regressed through all but one of the discordant grains and the concordant groups yields upper and lower intercept ages respectively at 3300 ± 3 Ma and 326 ± 129 Ma (Fig. 9A). This upper intercept age is within uncertainties of the weighted mean age of the concordant grains. Therefore, we consider the weighted mean age of 3299 ± 9 Ma to represent the crystallization age of the Bonai porphyritic granite. The $\varepsilon Hf_{(t)}$ values of the zircon grains range from −1.7 to +3.4 (Fig. 9D). Two-stage depleted mantle model ages (T_{DM2}) for the zircon grains from this sample, using mafic crust $^{176}Lu/^{177}Hf$ of 0.022, range from 3915 Ma to 3448 Ma (average = 3622 Ma).

4.2. Tamperkola rhyolite

Zircon grains in the Tamperkola rhyolite are pink-colored, euhedral and elongated prisms and range in size from 100 μm to 350 μm. In the CL images the zircon grains preserve oscillatory zoning (Fig. 5D). A few grains include overgrowth rims but inherited cores are not observed. Analytical spots (n = 40) are mostly placed on the outer growth zones in the CL images (Fig. 5D). Except for two zircon grains with high U (722 ppm and 355 ppm) and Th (589 ppm and 517 ppm) contents, the

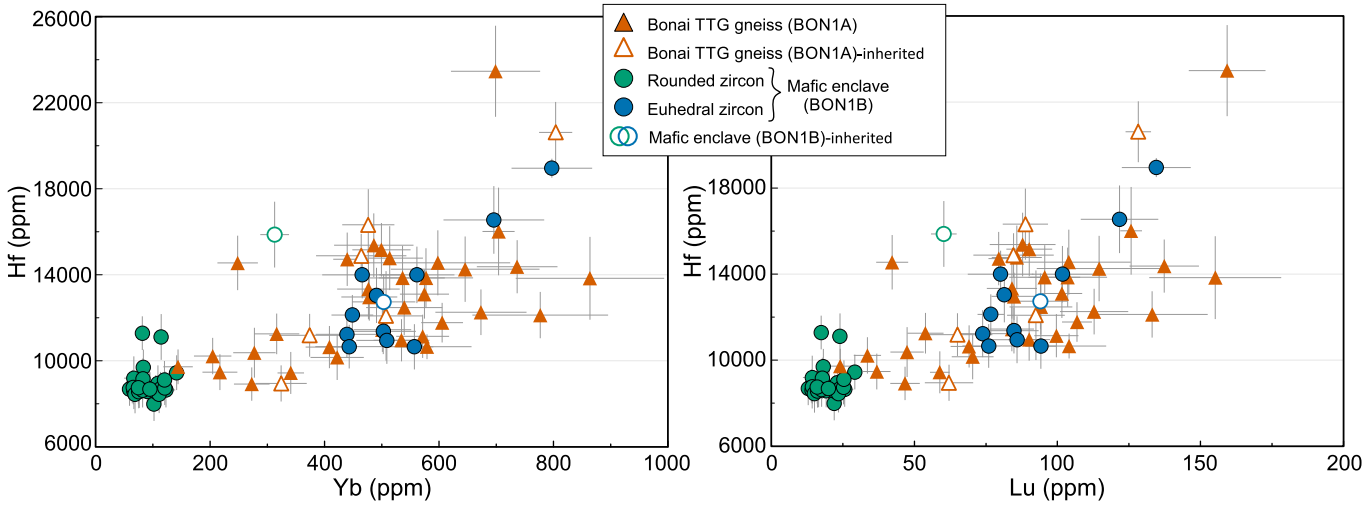

Fig. 8. Scatter plots showing lower concentrations of trace elements (Yb, Lu, and Hf) in the rounded zircon grains compared to the euhedral zircon grains within the mafic enclave. Note that the higher trace elements concentrations in the euhedral zircon grains mostly corresponds to the values observed in the zircon grains from the host Bonai TTG gneiss.

analyzed zircon grains have consistent U (44–136 ppm) and Th (24–113 ppm) contents and their Th/U ratios range from 0.54 to1.46 (Fig. 10A).

The majority (n = 38/40) of the analyzed grains yield concordant ages (discordance % = −1.1 to 2.9) and make a single group, with some grains slightly deviating from the concordia curve (Fig. 10A). The grains in this group have similar ages between 2837Ma to 2789 Ma and $^{176}Hf/^{177}Hf_{(t)}$ ratios between 0.280887 to 0.280941 (Fig. 10A–C) and define a weighted mean age at 2810 ± 8 Ma (Fig. 10B). Among the remaining two discordant grains (discordance % = 4 and 7.6), one grain slightly deviates from the concordant grains following a lead-loss pattern, and the other grain behaves as an outlier. The $^{176}Hf/^{177}Hf_{(2810\ Ma)}$ of these grains (0.280921 and 0.280940) is similar to those of the concordant grains (Fig. 10C), indicating that the discordance in the first grain is due to lead loss, and the anomalous U—Pb data of the second grain is potentially due to isotope disturbance. A discordia line regressed through all grains, excluding the outlier, yields upper and lower intercept ages respectively at 2814 ± 4 Ma and at the present time (Fig. 10A). The upper intercept age of the discordia is within uncertainties of the weighted mean age of the concordant grains. Thus, we consider the weighted mean age at 2810 ± 8 Ma to represent the crystallization age of the Tamperkola rhyolite. The $\varepsilon Hf_{(t)}$ values of the zircon grains range between −3.2 to −0.6 (Fig. 10D). Two-stage depleted mantle model ages (T_{DM2}) using mafic crust $^{176}Lu/^{177}Hf$ = 0.022 for the zircon grains in this sample range from 3709 Ma to 3493 Ma (average = 3616).

5. Discussion

5.1. Age, petrogenesis, and regional correlation of Bonai Suite

5.1.1. Crystallization age of Bonai Suite

The crystallization ages of the Bonai TTG gneiss (BON1A, 3316 ± 9 Ma) and porphyritic granite (BTNR1, 3299 ± 9 Ma) overlap within uncertainties (Figs. 6B and 9B), indicating that the two plutons were crystallized concurrently or with a very short gap. The two rock types also have similar Hf isotope compositions ($\varepsilon Hf_{(t)}$ = −0.2 to +4.6 for BON1A and −1.7 to +3.4 for BTNR1) and average T_{DM2} ages (BON1A = 3617 Ma and BTNR1 = 3622 Ma) (Figs. 6D and 9D), demonstrating a juvenile composition of the source magmas that was extracted from the depleted mantle at ca. 3622–3617 Ma.

5.1.2. Crystallization age of mafic enclave in Bonai TTG gneiss (BON1B)

The different morphologies and trace element concentrations of zircon grains in this sample, dominantly rounded and minor euhedral grains with lower and higher Yb, Lu, and Hf, respectively (Fig. 8), suggest crystallization from melts with different compositions. Both morphological groups show faint to well-developed internal growth zoning and high Th/U ratios (92 % of Th/U > 0.3), which lend support for crystallization from a melt (Figs. 5B and 7B and C; Corfu et al., 2003). The mafic enclave consists of a dominant mafic component with cross-cutting felsic veins (Fig. 3C). The anhedral zircon grains are likely crystallized within the mafic component of the enclave with an initially high zircon saturation, where zircon can only form during the latest stages of crystallization (≥ 70 % fractional crystallization) when the residual melt is enriched in Si and Zr and attains a lower zircon saturation (Watson and Harrison, 1983; Siégel et al., 2018; Shao et al., 2019; Gudelius et al., 2020; Bea et al., 2022; Scharf et al., 2023). Such delayed onset of zircon crystallization implies a short growth period in a spatially constrained melt, leading to formation of rounded zircon grains (Bea et al., 2006; Scharf et al., 2023). The late-stage anhedral zircon grains formed in the mafic melt, where early-crystallized amphibole with high partition coefficient for Yb, Lu, and Hf depleted the residual melt (Fujimaki, 1986; Rollinson, 1993; Rubatto, 2002), had lower amounts of these elements in the ambient melt to incorporate. Given that the intruding felsic veins in the enclave are compositionally similar to the host TTG rock (Fig. 3C), we suspect the euhedral zircon grains reside in these veins and crystallized from the felsic TTG melt. The high Zr and Si content and lower zircon saturation in the felsic melts facilitate the early onset of zircon crystallization (after ≥20 % fractional crystallization), allowing protracted growth with higher compositional and spatial freedom to develop a euhedral shape (Corfu et al., 2003; Siégel et al., 2018; Shao et al., 2019; Gudelius et al., 2020; Scharf et al., 2023). The early crystallization of these grains in the felsic melt, aided by the large partition coefficient of the mineral for REE and high field strength elements Yb, Lu, and Hf (Fujimaki, 1986; Rollinson, 1993; Rubatto, 2002) would allow the zircon grains to uptake more of these elements. Consistent with this interpretation, the higher Yb, Lu, and Hf contents in the euhedral zircon grains largely overlap with those of the zircon grains in the host TTG (Fig. 8). Alternatively, if the initial mafic melt reached zircon saturation and formed zircon grains in its early crystallization, the present rounded zircon grains may have resulted from resorption of these earlier zircon crystals due to changes in zircon saturation during subsequent magma recharge. In this scenario, the euhedral zircons could

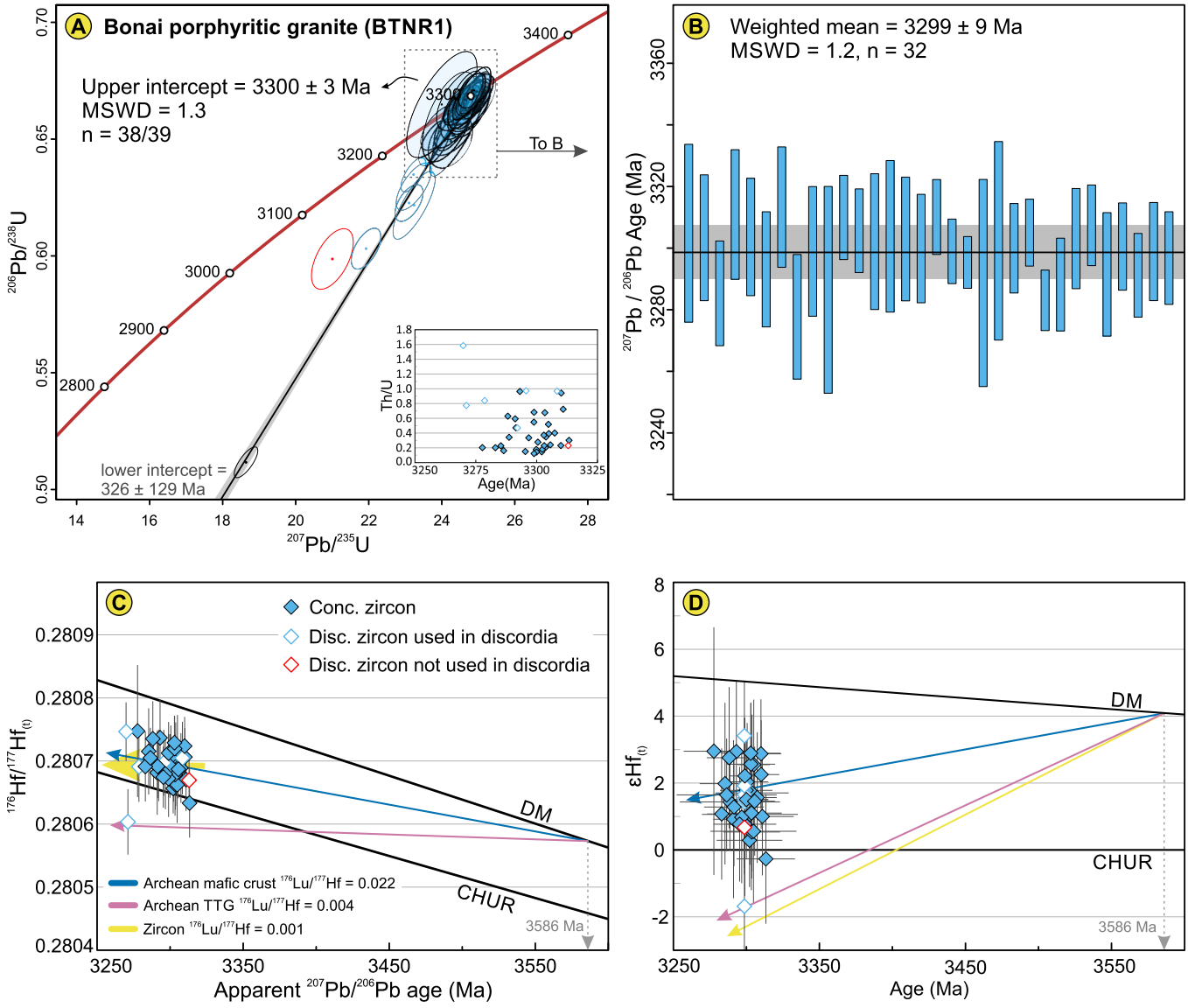

Fig. 9. (A) Zircon U—Pb concordia and Th/U scatter plot for zircon grains analyzed from the Bonai porphyritic granite. The grain with red outline is not included in calculating the discordia ages. B) Weighted mean age plot for the concordant zircon grains in this sample. C) Plot of initial $^{176}Hf/^{177}Hf$ versus measured ages for the zircon grains, showing similar Hf isotope compositions for discordant and concordant grains. D) Plot of $\varepsilon Hf_{(t)}$ values versus age demonstrates a dominantly suprachondritic Hf isotope signature for this rock. Note that in panels C and D the data from the Bonai porphyritic granite plot on the evolutionary array defined by a mafic crustal source with $^{176}Lu/^{177}Hf = 0.022$ and initiating at 3586 Ma age of the inherited zircon grains in the Bonai TTG gneiss. (For interpretation of the references to colour in this figure legend, the reader is referred to the web version of this article.)

have crystallized later, once the replenished system reached zircon saturation again.

The morphological and geochemical characteristics confirm that the rounded zircon grains are formed within the mafic enclave. Therefore, their weighted mean age at 3325 ± 9 Ma represents the crystallization age of the enclave. The suprachondritic Hf isotope compositions for the rounded zircon grains ($\varepsilon Hf_{(t)} = 0$ to +3.8; Fig. 7G) suggest a juvenile melt source with short crustal residence time. Given the consistent age and isotopic composition for the rounded and euhedral zircon grains (Fig. 7), excluding the euhedral grains does not change our interpretations. The two older grains in this sample (3424 Ma and 3405 Ma) follow the discordia pattern of the inherited grains in the host TTG rock and exhibit similar Hf isotope compositions to these grains (Fig. 7 B and F). Thus, we interpret these two grains as inherited and argue that the upper intercept age of ca. 3586 Ma from the inherited grains in the host TTG gneiss provide a reasonable crystallization age for these grains.

5.1.3. *Petrogenesis and regional correlation of Bonai Suite*

The crystallization age of the mafic enclave at 3325 ± 9 Ma is within uncertainties of the 3316 ± 9 Ma age of the host Bonai TTG gneiss, implying a very short gap in crystallization of the two rock types. The Hf isotope compositions of the *igneous* zircon grains (i.e., zircon grains crystallized from the melt) are identical between the two samples (96 % of $\varepsilon Hf_{(t)} = 0$ to +4) and consistently fall below the depleted mantle array (Fig. 11), suggesting magma derivation from older crustal source(s). Further confirming this interpretation is the presence of inherited zircon grains, i.e., remnants of the melted source, in both the host TTG and the mafic enclave. The upper intercept age of the inherited zircon grains at 3586 ± 25 Ma provides a tight estimate of the crystallization age for this potential crustal source (Fig. 6A), and their average $\varepsilon Hf_{(3586\ Ma)} = +4$ demonstrate that magma for this crustal source was derived from the depleted mantle (Fig. 11). Furthermore, the average T_{DM2} ages for the *igneous* zircon grains are similar between the Bonai TTG gneiss (average = 3617 Ma) and the mafic enclave (average = 3588 Ma), which are both

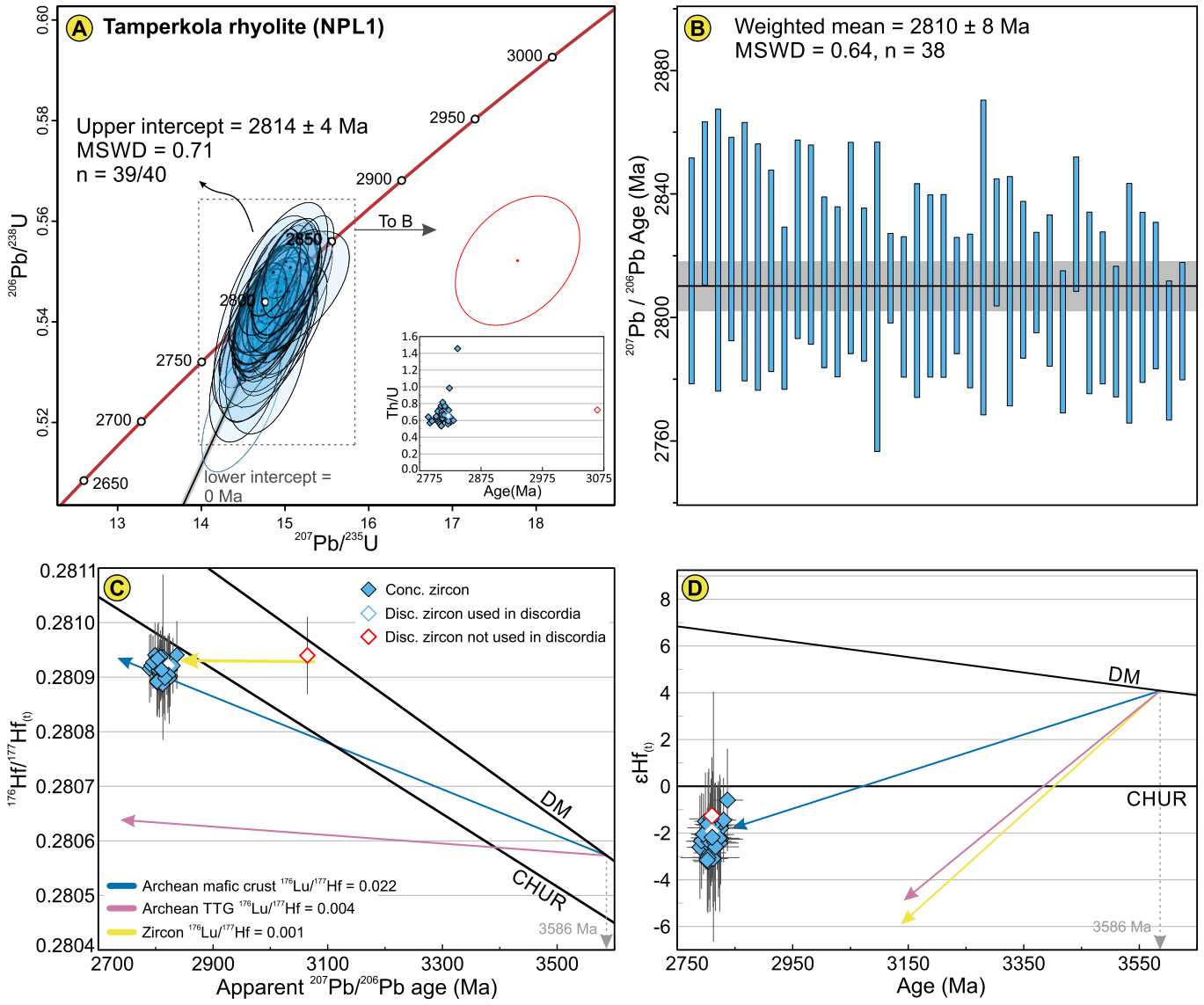

Fig. 10. Zircon U—Pb concordia and Th/U scatter plot for zircon grains analyzed from the Tamperkola rhyolite. The grain with red outline is not included in calculating the discordia ages. B) Weighted mean age plot for the concordant zircon grains in this sample. C) Plot of initial $^{176}Hf/^{177}Hf$ versus measured ages for the zircon grains, showing similar Hf isotope compositions for discordant and concordant grains. D) Plot of $\varepsilon Hf_{(t)}$ values versus age demonstrates subchondritic Hf isotope signature for this rock. Note that in panels C and D the data from the Tamperkola rhyolite plot on the evolutionary array defined by the Bonai Suite, initiating at ca. 3586 Ma and with $^{176}Lu/^{177}Hf = 0.022$. (For interpretation of the references to colour in this figure legend, the reader is referred to the web version of this article.)

within the range of the ca. 3586 Ma age of the inherited zircon grains. Although the sample from the Bonai porphyritic granite (BTNR1) does not contain inherited zircon grains, its age, Hf isotope composition (95 % of $\varepsilon Hf_{(t)} = 0$ to +4), and T_{DM2} (average = 3622 Ma) correspond to those of the Bonai TTG gneiss and its enclave (Fig. 11) and hence is compatible with these interpretations. The presented evidence collectively demonstrates that the different rock types in the Bonai Suite are derived from a shared source, which was itself extracted from the depleted mantle at ca. 3586 Ma. Although the mafic enclave might be a restite after partial melting and suggest a mafic composition for the predicted source rock, as discussed below, evidence for this is ambiguous. Independent evidence for a mafic composition for this crustal source is provided by the $^{176}Lu/^{177}Hf$ ratio from the Hf evolutionary array of the zircon grains in the Bonai Suite (Fig. 6D and 11B), yielding a value close to the Archean mafic crust (~0.022; Amelin et al., 1999). A mafic source for the Bonai Suite is also supported by whole-rock rare earth elements geochemistry of TTG enclaves in these rocks, which are interpreted to be derived from lower crust amphibolite sources with variable garnet content (Asokan et al., 2021). The presence of TTG enclaves in these rocks indicates that in addition to the mafic crustal source, partial melts from older TTG rocks also contributed minor amount of melt to the Bonai Suite magma. This is also shown by the relatively evolved and high potassium composition of the porphyritic granite variety of the Bonai Suite, which altogether indicate a transitional character for the Bonai Suite between Na-rich TTGs and K-rich granites (cf. Sengupta et al., 1991; Asokan et al., 2021).

Mafic microgranular enclaves are common within felsic granitoids and their origins have been continuously debated with the three most popular models include: (A) a disrupted cumulate of early-formed minerals (e.g., Dodge and Kistler, 1990; Dahlquist, 2002; Donaire et al., 2005; Gómez-Frutos and Castro, 2023), (B) mingling of non/cogenetic mafic and felsic magmas (e.g., Vernon, 1984; Barbarin and Didier, 1992), and (C) a residual (restite) after partial melting of a mafic source (e.g., White and Chappell, 1977; Chappell et al., 1987). Given the shared melt source for the three rocks type of the Bonai Suite, in the simplest scenario, the mafic enclave could represent a disrupted

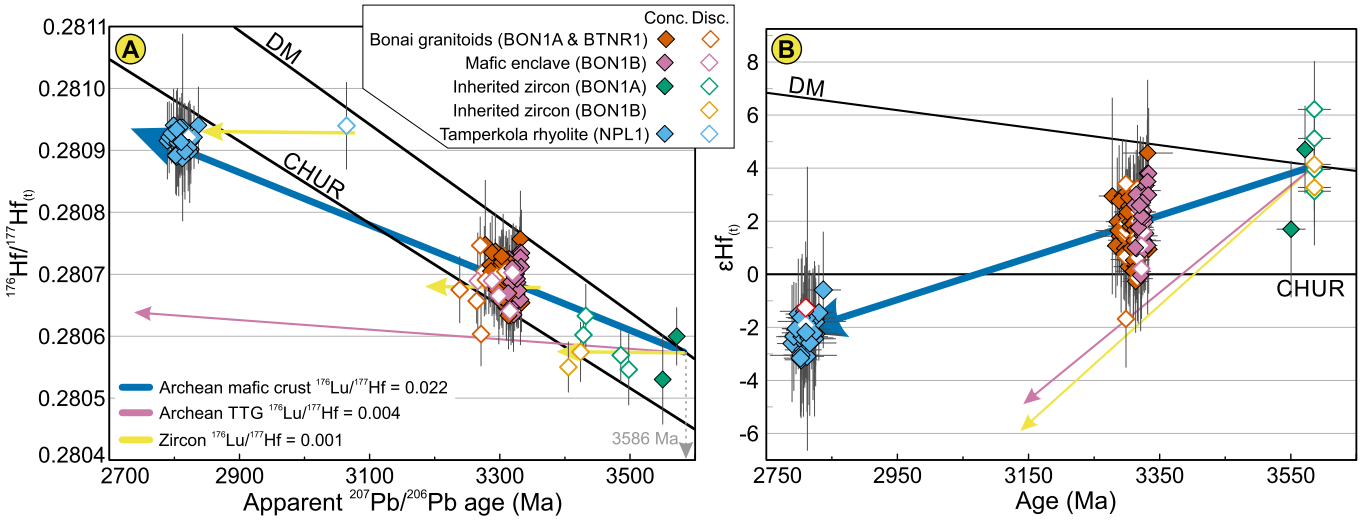

Fig. 11. Plots of initial $^{176}Hf/^{177}Hf_{(t)}$ (A) and $\varepsilon Hf_{(t)}$ (B) versus age of zircon grains from the Bonai and Tamperkola suites, showing that all of the samples follow the evolution array of a mafic crustal source indicated by the inherited zircon grains in the Bonai Suite, initiating at ca. 3586 Ma and with $^{176}Lu/^{177}Hf = 0.022$.

cumulate, and the Bonai TTG gneiss and porphyritic granite formed during later fractionation of the magma, which all happened in a very short period of time. However, the predominance of amphibole in the amphibolite enclave, and the complete absence of this mineral in the TTG host requires the crystal fractionation to be 100 % efficient in removing the mafic components from the melt into the cumulate. We consider this scenario unlikely, as previous studies show that mafic enclaves of cumulate origin are largely restricted to granitoids that have similar mineralogy to the enclosing enclaves with only the proportions of the phases being different between the two rocks (e.g., Dodge and Kistler, 1990; Dahlquist, 2002; Gómez-Frutos and Castro, 2023).

Both the magma mingling and the restite models suggest that the felsic TTG melt was likely derived from partial melting of the mafic crustal source, and the essential difference between the two models is the phase state of the mafic enclave, i.e., whether it ascended as a mafic melt or as a solid residue? The occurrence of the mafic enclaves as both rounded to elongated xenoliths and schlieren bands (Fig. 3C and D) indicates it was substantially liquid and flowed with the host felsic magma (cf. Vernon, 1984; Vernon et al., 1988). In addition, the very short gap in crystallization of *igneous* zircon grains in both the mafic enclave and host TTG further support a substantially liquid state for the mafic enclave. Therefore, mingling of felsic and mafic magmas can best explain the occurrence of the mafic enclaves within the Bonai TTG gneiss. Given the shared mafic crustal source for all rock types in the Bonai Suite, the magma mingling model for the TTG gneiss and its mafic enclaves would require two distinct partial melting and melt extraction episodes from this source, which would most likely be in disequilibrium and expected to react upon blending. However, the absence of pervasive reaction and chemical mixing (different mineralogy of the rocks) of the two melts, indicates that they were relatively cool at the time of blending.

5.1.4. Regional correlation of Bonai Suite

The age, isotopic signature, and composition of the Bonai Suite corresponds to the middle phase (Singhbhum Suite) of the Singhbhum Granitoid Complex of Hofmann et al. (2022). This middle phase includes syn-tectonic deformed and undeformed suites with ca. 3350–3250 Ma crystallization ages and variable compositions from tonalite to granodiorite and granite with dominantly juvenile isotopic compositions. Therefore, despite the absence of direct geographic link between the two rock suites, the Bonai Suite represents the westward extension of the SGC (Fig. 1).

5.2. Age, petrogenesis, and regional correlation of Tamperkola Suite

The weighted mean age at 2810 ± 8 Ma (Fig. 10B) provides a reliable crystallization age for the Tamperkola rhyolite. This age is within uncertainties of the 2809 ± 9 Ma age of the associated Tamperkola granite (Bandyopadhyay et al., 2001), and indicates concurrent crystallization of the Tamperkola Suite. The subchondritic $\varepsilon Hf_{(t)}$ (−3.2 to −0.6; Fig. 10D) of the Tamperkola rhyolite indicate the role of crustal reworking in the magma genesis for this rock. On the $\varepsilon Hf_{(t)}$ versus age diagram the data from the Tamperkola rhyolite plot on the evolutionary array defined by the igneous and inherited zircon grains in the Bonai Suite (Fig. 11), suggesting that the magma for this rhyolite is likely originated from melting of the local Bonai TTG-granite Suite and that no mantle input was required. Although the TTGs derived directly from partial melting of the Archean mafic crust are not deemed sufficiently potassic to generate granitic melts (Watkins et al., 2007; White et al., 2017), the transitional character of the Bonai TTG-granite Suite with elevated K content is sufficiently fertile to generate high-K granitic melt upon its (partial) melting (cf. Rollinson et al., 2024). Although we do not find inherited zircon grains in the Tamperkola rhyolite, Bandyopadhyay et al. (2001) reported zircon grains with ages between 3300 Ma to 3200 Ma from the associated Tamperkola granite, which conform with the crystallization age of the Bonai Suite and hence confirming our interpretations.

Contemporaneous (ca. 2800 Ma) and similarly deformed granitic and charnockitic gneisses with A-type geochemical attributes are also widespread to the south of our study area in the Rengali Province (Misra et al., 2000; Nelson et al., 2014; Chattopadhyay et al., 2015; Bose et al., 2016; Dasgupta et al., 2017; Topno et al., 2018). The limited Hf isotope data from these rocks (two zircon grains $\varepsilon Hf_{(t)}$ values at −2.5 and +0.1; Topno et al., 2018) agree with that of the Tamperkola rhyolite and plot on the Hf-time evolutionary array defined by the data from the Bonai Suite. Furthermore, the geochemical characteristics for the ca. 2800 Ma metaigneous rocks in the Rengali Province are interpreted to indicate a melt source from shallow partial melting of a tonalitic/granodioritic source rock (Topno et al., 2018). Therefore, the age and geochemical characteristic of the ca. 2800 Ma felsic metaigneous rocks in the Rengali Province are similar to those of the Tamperkola Suite and indicate melt derivation from reworking of the local crust with possible TTG composition and isotope signature akin to those of the Bani Suite. The tectonothermal event responsible for this crustal melting episode remains elusive, with contradictory models involving a dominantly extensional regime across the entire craton (Topno et al., 2018) to localized within-

plate extension in a convergent setting (Dasgupta et al., 2017), and a primarily convergent orogen in the SW margin of the craton (Bose et al., 2016) are suggested.

5.3. Implications for Archean crustal evolution

The new data suggest that the magma for the Bonai Suite was derived from a ca. 3586 Ma crustal source with mafic composition and juvenile Hf isotope composition (mean $\varepsilon Hf_{(3586\ Ma)} = +4 \pm 1.8$). Mafic volcanic rocks are exposed in both the lower and upper lava units of the W-IOG bordering the Bonai Suite to the east (Fig. 1). The imprecise Sm—Nd age reported from the lower lava flow (3420 ± 140 Ma) does not overlap with the age of the mafic crustal source for the Bonai Suite (Wright and Basu, 2024). However, their mafic composition and mantle-like isotopic signature ($\varepsilon Nd_{(3586\ Ma)} = +6.6 \pm 2.5$) are consistent with those of the mafic source for the Bonai Suite (Wright and Basu, 2024). On this basis, we hypothesize that mafic rocks, similar to the juvenile mafic lavas of the W-IOG, were deeply buried and served as a source for the Bonai Suite. If this interpretation is correct, the early Paleoarchean crystallization age of ca. 3586 Ma for this mafic source, as evidenced by the inherited zircon grains age, and its subsequent (partial) melting in the late Paleoarchean (i.e., ca. 3316–3299 Ma emplacement age of Bonai Suite) suggests a crustal residence time of ca. 300 Myr for the Archean mafic lower crust in the Singhbhum Craton. This is similar to the Archean mafic lower crust residence time of several 100 Myr interpreted for the Bastar Craton (Maltese et al., 2021), but shorter than the ca. 500 Myr interpreted for the Slave Craton (Pietranik et al., 2008).

The TTG-granite composition for the Bonai Suite, and its isotopic composition plotting on the evolutionary array of the predicted mafic crust with a Lu/Hf = 0.022 (Fig. 11), is interpreted here to be achieved by partial melting of the indicated mafic crustal source with limited contribution from older juvenile TTG rocks and without mantle input. Similarly bulk-rock and isotopic composition of the Tamperkola Suite can be achieved by sole (partial) melting of the local transitional TTGs similar to the Bonai TTG-granite Suite. These observations collectively demonstrate a three-step crustal reworking process in the western part of the Singhbhum Craton, which played the main role in cratonic crust fractionation and maturation. These include (i) the early formation of depleted mantle-derived mafic rocks at ca. 3586 Ma, (ii) their subsequent residence for ca. 300 Myr and melting to form intermediate TTG and felsic granitic rocks at ca. 3316–3299 Ma, and (iii) melting of the TTG-granite crust to produce the high-K granites at ca. 2810 Ma (Figs. 11 and 12). Our data does not require, or even precludes, the involvement of any mantle-derived melts, suggesting that geodynamic forces, such as crustal burial, crustal tectonic staging or some form of dripduction triggered the cannibalistic reworking of the crust (e.g., Johnson et al., 2014; Nebel et al., 2018; Nebel et al., 2024).

Mafic greenstones belts, TTG-granite suites, and high-K granites form the dominant lithologies in many cratons worldwide from the Paleoarchean to Neoarchean, e.g., Pilbara, Dharwar, and Kaapvaal cratons and the Superior Province (Laurent et al., 2014; Nebel et al., 2018; Chaudhuri, 2020; Cawood et al., 2022). The felsic magmatic rocks in these cratons exhibit a consistent compositional evolution. The initial stage of felsic magmatism marks the appearance of the TTG suites, which exhibit low K for a given Na content and are emplaced into, or partially contemporaneous with, greenstone belts. These are succeeded by voluminous TTG-granite suites (transitional TTGs) with elevated K content, often exhibiting mingling between TTG and granitic compositions, indicating melt derivation from both mafic crust and TTG sources (Nebel et al., 2018). The subsequent magmatic stage is characterized by high-K granites, also referred to as Archean crustal progeny (ACP) or biotite-granites, which have elevated contents of large ion lithophile elements (LILE, e.g., K, Rb, Ba, and Th), suggesting melt derivation from sources with high concentrations of LILEs. Although these magmatic stages may not occur simultaneously across all cratons, the sequence of compositional evolution remains consistent. Given the appearance of high-K granites in global cratons from Mesoarchean to Neoarchean times following the transitional TTGs (Laurent et al., 2014; Cawood et al., 2018; Cawood et al., 2022; Rollinson et al., 2024), the crustal maturation observed in the western Singhbhum Craton might be a common process of crustal evolution. In this model, K-enriched transitional TTGs bridge the compositional gap between TTGs and high-K granites, which, at least in our case, does not require the involvement of buried sedimentary successions, as has recently been proposed (Reimink and Smye, 2024).

6. Conclusion

The age and isotopic data indicate that the Bonai Suite to the west of the Western Iron Ore Group belongs to the Singhbhum Granitoid Suite occupying the core of the craton. The Tamperkola Suite represents northward extension of the granitic magmatism that affected the Rengali Province at ca. 2800 Ma. The age and isotopic composition of the Bonai and Tamperkola suites, together with published data from the lower lava flows of the W-IOG, demonstrate episodic crustal reworking between ca. 3586 Ma to ca. 2810 Ma in the western part of the

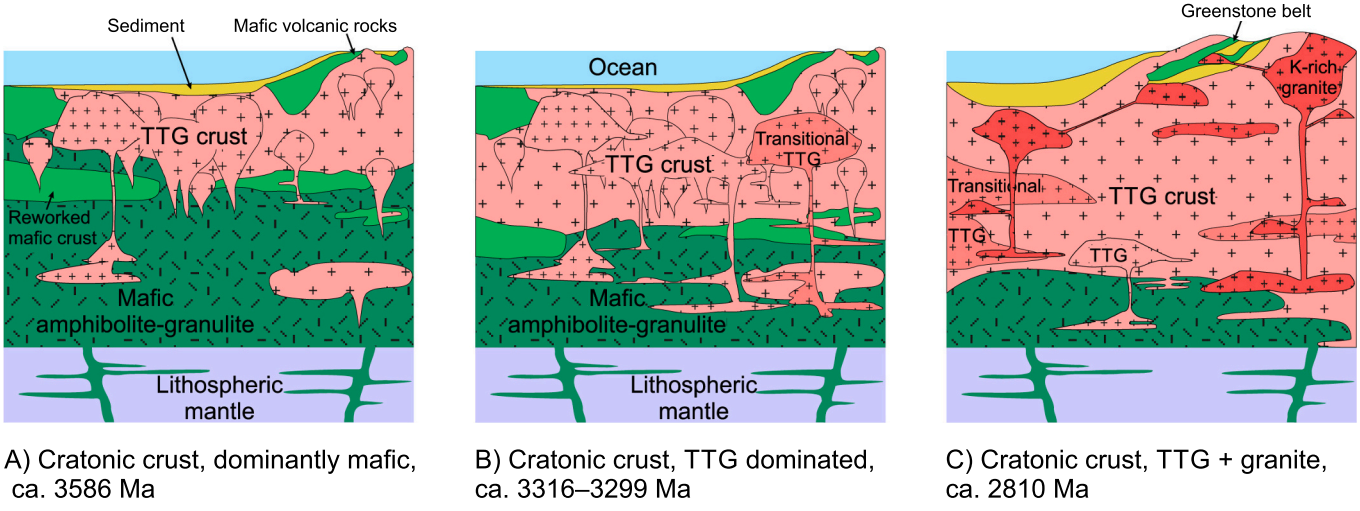

Fig. 12. Schematic crustal sections of the Archean cratonic crust, modified from Cawood et al. (2022), showing the three-step crustal reworking processes in the western part of the Singhbhum Craton starting with (A) formation of the mafic crust at ca. 3586 Ma, (B) partial melting of the mafic crust and older TTGs at ca. 3316–3299 Ma to generate the TTG-granite suites (transitional TTGs), and (C) partial melting of the TTG-granite crust at ca. 2810 Ma to form the high-K magmas.

Singhbhum Craton, which has played the main role in crustal fractionation and transition from mafic to intermediate and felsic crust. This three-step evolution in a confined, regional context demonstrates the crucial role of internal crustal reworking to generate evolved, continental crust-like igneous successions.

CRediT authorship contribution statement

Yousef Zoleikhaei: Writing – review & editing, Writing – original draft, Visualization, Methodology, Investigation, Formal analysis, Data curation, Conceptualization. **Trisrota Chaudhuri:** Writing – review & editing, Writing – original draft, Investigation, Conceptualization. **Peter A. Cawood:** Writing – review & editing, Validation, Supervision, Funding acquisition, Conceptualization. **Rajat Mazumder:** Writing – review & editing, Resources, Funding acquisition. **Oliver Nebel:** Writing – review & editing, Visualization, Investigation. **Shuvabrata De:** Visualization, Resources.

Declaration of competing interest

The authors declare that they have no known competing financial interests or personal relationships that could have appeared to influence the work reported in this paper.

Data availability

The data that supports the findings of this study are available in the supplementary material of this article.

Acknowledgements

Fieldwork for this study was supported by the Indian Statistical Institute Kolkata (2010-2011 sessions), the Research Council of Oman (TRC) Block Funding (BF) 2020 (2021-2022 sessions), TRC BF 2023, and GUtech Seed Funding 2023-2025 (2023 session). Laboratory analyses were supported by the Australian Research Council grant FL160100168. The authors would like to thank Junnel Alegado, Massimo Raveggi, and Rachelle Pierson (Monash University) and Graham Hutchinson (University of Melbourne) for their assistance with laboratory analyses. We extend our gratitude to Hugo Olierook and an anonymous reviewer for their constructive comments, and to Marco Fiorentini for efficient editorial handling.

Appendix A. Supplementary data

Supplementary data to this article can be found online at https://doi.org/10.1016/j.chemgeo.2024.122483.

References

Acharyya, S.K., Gupta, A., Orihashi, Y., 2010. New U-Pb zircon ages from Paleo-Mesoarchean TTG gneisses of the Singhbhum Craton, Eastern India. Geochem. J. 44 (2), 81–88. https://doi.org/10.2343/geochemj.1.0046.

Alam, P., Tripathi, S., Agarwal, M., Sinha, D.K., 2022. Partition coefficient as pathfinder for uranium mineralization: Case studies from Tamperkola granite and Soda granite, Singhbhum Craton, India. Explorat. Res. Atom. Min. 154–168.

Amelin, Y., Lee, D.-C., Halliday, A.N., Pidgeon, R.T., 1999. Nature of the Earth's earliest crust from hafnium isotopes in single detrital zircons. Nature 399 (6733), 252–255. https://doi.org/10.1038/20426.

Asokan, A.D., Mahapatro, S.N., Ram Mohan, M., Rocholl, A., Wiedenbeck, M., Nanda, J. K., 2021. Paleoarchean evolution of the Singhbhum Craton, eastern India: New constraints from geochemistry and geochronology of granitoids of Bonai and Champua area. Precambrian Res. 366, 106429. https://doi.org/10.1016/j.precamres.2021.106429.

Bandyopadhyay, P.K., Chakrabarti, A.K., DeoMurari, M.P., Misra, S., 2001. 2.8 Ga Old Anorogenic Granite-Acid Volcanics Association from Western margin of the Singhbhum-Orissa Craton, Eastern India. Gondw. Res. 4 (3), 465–475. https://doi.org/10.1016/S1342-937X(05)70346-4.

Barbarin, B., Didier, J., 1992. Genesis and evolution of mafic microgranular enclaves through various types of interaction between coexisting felsic and mafic magmas. Earth Environ. Sci. Trans. R. Soc. Edinb. 83 (1–2), 145–153. https://doi.org/10.1017/S0263593300007835.

Barley, M.E., Pickard, A.L., 1999. An extensive, crustally-derived, 3325 to 3310 Ma silicic volcanoplutonic suite in the eastern Pilbara Craton: evidence from the Kelly Belt, McPhee Dome and Corunna Downs Batholith. Precambrian Res. 96 (1), 41–62. https://doi.org/10.1016/S0301-9268(99)00003-0.

Bea, F., Montero, P., Ortega, M., 2006. A LA–ICP–MS evaluation of Zr reservoirs in common crustal rocks: implications for Zr and hf geochemistry, and zircon-forming processes. Can. Mineral. 44 (3), 693–714. https://doi.org/10.2113/gscanmin.44.3.693.

Bea, F., Bortnikov, N., Cambeses, A., Chakraborty, S., Molina, J.F., Montero, P., Morales, I., Silantiev, S., Zinger, T., 2022. Zircon crystallization in low-Zr mafic magmas: possible or impossible? Chem. Geol. 602, 120898. https://doi.org/10.1016/j.chemgeo.2022.120898.

Belcher, R.W., Kisters, A.F.M., 2006. Syntectonic emplacement and deformation of the Heerenveen batholith: Conjectures on the structural setting of the 3.1 Ga granite magmatism in the Barberton granite-greenstone terrain, South Africa. In: Reimold, W.U., Gibson, R.L. (Eds.), Processes on the Early Earth, vol. 405. Geological Society of America, p. 0.

Black, L.P., Kamo, S.L., Williams, I.S., Mundil, R., Davis, D.W., Korsch, R.J., Foudoulis, C., 2003. The application of SHRIMP to Phanerozoic geochronology; a critical appraisal of four zircon standards. Chem. Geol. 200 (1), 171–188. https://doi.org/10.1016/S0009-2541(03)00166-9.

Bose, S., Das, K., Kimura, K., Hidaka, H., Dasgupta, A., Ghosh, G., Mukhopadhyay, J., 2016. Neoarchean tectonothermal imprints in the Rengali Province, eastern India and their implication on the growth of Singhbhum Craton: evidence from zircon U–Pb SHRIMP data. J. Metam. Geol. 34 (8), 743–764. https://doi.org/10.1111/jmg.12201.

Bouvier, A., Vervoort, J.D., Patchett, P.J., 2008. The Lu–Hf and Sm–Nd isotopic composition of CHUR: Constraints from unequilibrated chondrites and implications for the bulk composition of terrestrial planets. Earth Planet. Sci. Lett. 273 (1), 48–57. https://doi.org/10.1016/j.epsl.2008.06.010.

Cawood, P.A., Hawkesworth, C.J., Dhuime, B., 2013. The continental record and the generation of continental crust. GSA Bull. 125 (1–2), 14–32. https://doi.org/10.1130/B30722.1.

Cawood, P.A., Hawkesworth, C.J., Pisarevsky, S.A., Dhuime, B., Capitanio, F.A., Nebel, O., 2018. Geological archive of the onset of plate tectonics. Philos. Trans. R. Soc. A Math. Phys. Eng. Sci. 376 (2132), 20170405. https://doi.org/10.1098/rsta.2017.0405.

Cawood, P.A., Chowdhury, P., Mulder, J.A., Hawkesworth, C.J., Capitanio, F.A., Gunawardana, P.M., Nebel, O., 2022. Secular evolution of continents and the earth system. Rev. Geophys. 60 (4), e2022RG000789. https://doi.org/10.1029/2022RG000789.

Chakraborti, T.M., Ray, A., Deb, G.K., Upadhyay, D., Chakrabarti, R., 2019. Evidence of crustal reworking in the Mesoarchean: Insights from geochemical, U-Pb zircon and Nd isotopic study of a 3.08–3.12 Ga ferro-potassic granite-gneiss from north-eastern margin of Singhbhum Craton, India. Lithos 330-331, 16–34. https://doi.org/10.1016/j.lithos.2019.01.026.

Chakraborty, T., Upadhyay, D., Ranjan, S., Pruseth, K.L., Nanda, J.K., 2019. The geological evolution of the Gangpur Schist Belt, eastern India: Constraints on the formation of the Greater Indian Landmass in the Proterozoic. J. Metam. Geol. 37 (1), 113–151. https://doi.org/10.1111/jmg.12452.

Champion, D., Smithies, R., 2001. Archaean granites of the Yilgarn and Pilbara cratons, Western Australia. In: Cassidy, K.F., Dunphy, J.M., Van Kranendonk, M.J. (Eds.), 4th International Archaean Symposium 2002, Extended Abstracts. AGSO-Geoscience Australia, pp. 134–136.

Champion, D.C., Smithies, R.H., 2019. Chapter 21 - Geochemistry of Paleoarchean Granites of the East Pilbara Terrane, Pilbara Craton, Western Australia: Implications for early Archean Crustal Growth. In: Van Kranendonk, M.J., Bennett, V.C., Hoffmann, J.E. (Eds.), Earth's Oldest Rocks, Second edition. Elsevier, pp. 487–518.

Chappell, B.W., White, A.J.R., Wyborn, D., 1987. The importance of residual source material (restite) in granite petrogenesis. J. Petrol. 28 (6), 1111–1138. https://doi.org/10.1093/petrology/28.6.1111.

Chattopadhyay, S., Upadhyay, D., Nanda, J.K., Mezger, K., Pruseth, K.L., Berndt, J., 2015. Proto-India was a part of Rodinia: evidence from Grenville-age suturing of the Eastern Ghats Province with the Paleoarchean Singhbhum Craton. Precambrian Res. 266, 506–529. https://doi.org/10.1016/j.precamres.2015.05.030.

Chaudhuri, T., 2020. A review of Hadean to Neoarchean crust generation in the Singhbhum Craton, India and possible connection with Pilbara Craton, Australia: the geochronological perspective. Earth Sci. Rev. 202, 103085. https://doi.org/10.1016/j.earscirev.2020.103085.

Chaudhuri, T., Wan, Y., Mazumder, R., Ma, M., Liu, D., 2018. Evidence of enriched, hadean mantle reservoir from 4.2-4.0 ga zircon xenocrysts from paleoarchean TTGS of the singhbhum craton, Eastern India. Sci. Rep. 8 (1), 7069. https://doi.org/10.1038/s41598-018-25494-6.

Chaudhuri, T., Kamei, A., Das, M., Mazumder, R., Owada, M., 2022. Evolution of the Archean felsic crust of Singhbhum Craton, India: a reassessment. Earth-Sci. Rev. 231, 104067. https://doi.org/10.1016/j.earscirev.2022.104067.

Chu, N.-C., Taylor, R.N., Chavagnac, V., Nesbitt, R.W., Boella, R.M., Milton, J.A., German, C.R., Bayon, G., Burton, K., 2002. Hf isotope ratio analysis using multi-collector inductively coupled plasma mass spectrometry: an evaluation of isobaric interference corrections. J. Anal. At. Spectrom 17 (12), 1567–1574. https://doi.org/10.1039/B206707B.

Corfu, F., Hanchar, J.M., Hoskin, P.W.O., Kinny, P., 2003. Atlas of Zircon textures. Rev. Mineral. Geochem. 53 (1), 469–500. https://doi.org/10.2113/0530469.

Dahlquist, J.A., 2002. Mafic microgranular enclaves: early segregation from metaluminous magma (Sierra de Chepes), Pampean Ranges, NW Argentina. J. South Am. Earth Sci. 15 (6), 643–655. https://doi.org/10.1016/S0895-9811(02)00112-8.

Dasgupta, A., Bose, S., Das, K., Ghosh, G., 2017. Petrological and geochemical evolution of the Central Gneissic Belt, Rengali Province, eastern India: Implications for the Neoarchean growth and orogenesis. J. Asian Earth Sci. 146, 1–19. https://doi.org/10.1016/j.jseaes.2017.04.024.

Dey, S., Topno, A., Liu, Y., Zong, K., 2017. Generation and evolution of Palaeoarchaean continental crust in the central part of the Singhbhum craton, eastern India. Precambrian Res. 298, 268–291. https://doi.org/10.1016/j.precamres.2017.06.009.

Dey, S., Mitra, A., Nandy, J., Mondal, S., Topno, A., Liu, Y., Zong, K., 2019. Chapter 30 - early Crustal Evolution as Recorded in the Granitoids of the Singhbhum and Western Dharwar Cratons. In: Van Kranendonk, M.J., Bennett, V.C., Hoffmann, J.E. (Eds.), Earth's Oldest Rocks, Second edition. Elsevier, pp. 741–792.

Dodge, F.C.W., Kistler, R.W., 1990. Some additional observations on inclusions in the granitic rocks of the Sierra Nevada. J. Geophys. Res. Solid Earth 95 (B11), 17841–17848. https://doi.org/10.1029/JB095iB11p17841.

Donaire, T., Pascual, E., Pin, C., Duthou, J.-L., 2005. Microgranular enclaves as evidence of rapid cooling in granitoid rocks: the case of the Los Pedroches granodiorite, Iberian Massif, Spain. Contrib. Mineral. Petrol. 149 (3), 247–265. https://doi.org/10.1007/s00410-005-0652-0.

Farina, F., Albert, C., Lana, C., 2015. The Neoarchean transition between medium- and high-K granitoids: Clues from the Southern São Francisco Craton (Brazil). Precambrian Res. 266, 375–394. https://doi.org/10.1016/j.precamres.2015.05.038.

Fisher, C.M., Hanchar, J.M., Samson, S.D., Dhuime, B., Blichert-Toft, J., Vervoort, J.D., Lam, R., 2011. Synthetic zircon doped with hafnium and rare earth elements: a reference material for in situ hafnium isotope analysis. Chem. Geol. 286 (1), 32–47. https://doi.org/10.1016/j.chemgeo.2011.04.013.

Fisher, C.M., Vervoort, J.D., DuFrane, S.A., 2014. Accurate Hf isotope determinations of complex zircons using the "laser ablation split stream" method. Geochem. Geophys. Geosyst. 15 (1), 121–139. https://doi.org/10.1002/2013GC004962.

Fujimaki, H., 1986. Partition coefficients of Hf, Zr, and REE between zircon, apatite, and liquid. Contrib. Mineral. Petrol. 94 (1), 42–45. https://doi.org/10.1007/BF00371224.

Ghose, N.C., Saha, A., 2019. Vestiges of older greenstone in Mesoarchaean Chakradharpur granite gneiss, Singhbhum Craton, India: Implications for plume-lithosphere interaction at rifted cratonic margin. Geol. J. 54 (4), 1927–1949. https://doi.org/10.1002/gj.3271.

Gómez-Frutos, D., Castro, A., 2023. Mafic microgranular enclaves (MMEs) trace the origin of post-collisional magmas. Geology 51 (8), 743–747. https://doi.org/10.1130/G51248.1.

Gudelius, D., Zeh, A., Wilson, A.H., 2020. Zircon formation in mafic and felsic rocks of the Bushveld complex, South Africa: Constraints from composition, zoning, Th/U ratios, morphology, and modelling. Chem. Geol. 546, 119647. https://doi.org/10.1016/j.chemgeo.2020.119647.

Guitreau, M., Blichert-Toft, J., Martin, H., Mojzsis, S.J., Albarède, F., 2012. Hafnium isotope evidence from Archean granitic rocks for deep-mantle origin of continental crust. Earth Planet. Sci. Lett. 337-338, 211–223. https://doi.org/10.1016/j.epsl.2012.05.029.

Hawkesworth, C.J., Cawood, P.A., Dhuime, B., Kemp, T.I.S., 2017. Earth's Continental Lithosphere through Time. Ann. Rev. Earth Planet. Sci. 45 (2017), 169–198. https://doi.org/10.1146/annurev-earth-063016-020525.

Hofmann, A., Mazumder, R., 2015. Chapter 7 a review of the current status of the older Metamorphic Group and older Metamorphic Tonalite Gneiss: insights into the Palaeoarchaean history of the Singhbhum craton, India. Geol. Soc. Lond. Mem. 43 (1), 103–107. https://doi.org/10.1144/M43.7.

Hofmann, A., Jodder, J., Xie, H., Bolhar, R., Whitehouse, M., Elburg, M., 2022. The Archaean geological history of the Singhbhum Craton, India – a proposal for a consistent framework of craton evolution. Earth-Sci. Rev. 228, 103994. https://doi.org/10.1016/j.earscirev.2022.103994.

Horstwood, M.S.A., Košler, J., Gehrels, G., Jackson, S.E., McLean, N.M., Paton, C., Pearson, N.J., Sircombe, K., Sylvester, P., Vermeesch, P., Bowring, J.F., Condon, D.J., Schoene, B., 2016. Community-derived Standards for LA-ICP-MS U-(Th-)Pb geochronology – uncertainty propagation, age interpretation and data reporting. Geostand. Geoanal. Res. 40 (3), 311–332. https://doi.org/10.1111/j.1751-908X.2016.00379.x.

Jackson, S.E., Pearson, N.J., Griffin, W.L., Belousova, E.A., 2004. The application of laser ablation-inductively coupled plasma-mass spectrometry to in situ U–Pb zircon geochronology. Chem. Geol. 211 (1), 47–69. https://doi.org/10.1016/j.chemgeo.2004.06.017.

Jana, A., Sinha, D.K., 2021. Geochemistry and tectonic setting for the deposition of IOG siliciclastics at the western margin of Bonai Granite, Singhbhum-Orissa Craton, India. J. Indian Assoc. Sedimentol. 38 (2), 49–62. https://doi.org/10.51710/jias.v38i2.134.

Jana, A., Sarkar, B.C., Kumar, S., Kumar, A., Yadav, G.S., Kumar, P., 2016. Gold and uranium occurrences in quartz - pebble conglomerate of Iron Ore Group, Bagiyabahal - Baratangra area, Sundargarh district, Odisha, India. Curr. Sci. 111 (12), 1917–1921 https://www.i-scholar.in/index.php/CURS/article/view/129366.

Jodder, J., Hofmann, A., Ueckermann, H., 2021. 3.51 Ga old felsic volcanic rocks and carbonaceous cherts from the Gorumahisani Greenstone Belt – Insights into the Palaeoarchaean record of the Singhbhum Craton, India. Precambrian Res. 357, 106109. https://doi.org/10.1016/j.precamres.2021.106109.

Jodder, J., Hofmann, A., Xie, H., Elburg, M.A., Wilson, A., 2023. Geochronology of the Daitari Greenstone Belt, Singhbhum Craton. India. Precambrian Res. 388, 106997. https://doi.org/10.1016/j.precamres.2023.106997.

Johnson, T.E., Brown, M., Kaus, B.J.P., VanTongeren, J.A., 2014. Delamination and recycling of Archaean crust caused by gravitational instabilities. Nat. Geosci. 7 (1), 47–52. https://doi.org/10.1038/ngeo2019.

Kumar, A., Birua, S.N.S., Pande, D., Nath, A.R., Ramesh Babu, P.V., Pandit, S.A., 2009. Radioactive quartz-pebble conglomerates from western margin of Bonai granite pluton, Sundargarh district, Orissa — a new find. J. Geol. Soc. India 73 (4), 537–542. https://doi.org/10.1007/s12594-009-0037-5.

Kumar, A., Venkatesh, A.S., Ramesh Babu, P.V., Nayak, S., 2012. Genetic implications of rare uraninite and pyrite in quartz-pebble conglomerates from Sundargarh district of Orissa, Eastern India. J. Geol. Soc. India 79 (3), 279–286. https://doi.org/10.1007/s12594-012-0040-0.

Laurent, O., Martin, H., Moyen, J.F., Doucelance, R., 2014. The diversity and evolution of late-Archean granitoids: evidence for the onset of "modern-style" plate tectonics between 3.0 and 2.5Ga. Lithos 205, 208–235. https://doi.org/10.1016/j.lithos.2014.06.012.

Maltese, A., Mezger, K., Upadhyay, D., Berndt, J., Scherer, E.E., 2021. On the petrogenesis of Paleoarchean continental crust: U-Pb-Hf isotope and major-trace element constraints from the Bastar Craton, India. Chem. Geol. 579, 120337. https://doi.org/10.1016/j.chemgeo.2021.120337.

Mazumder, R., Chaudhuri, T., 2021. Paleoarchean terrestrial to shallow marine sedimentation on Singhbhum Craton, eastern India (the Western Iron Ore Group). Precambrian Res. 354, 106071. https://doi.org/10.1016/j.precamres.2020.106071.

Mazumder, R., Van Loon, A.J., Mallik, L., Reddy, S.M., Arima, M., Altermann, W., Eriksson, P.G., De, S., 2012. Mesoarchaean–Palaeoproterozoic stratigraphic record of the Singhbhum crustal province, eastern India: a synthesis. Geol. Soc. Lond. Spec. Publ. 365 (1), 31–49. https://doi.org/10.1144/SP365.3.

Mazumder, R., Chaudhuri, T., Biswas, S., 2019. Palaeoarchaean sedimentation and magmatic processes in the eastern Iron Ore Group, eastern India: a commentary. Geol. J. 54 (5), 3078–3087. https://doi.org/10.1002/gj.3479.

Mazumder, R., Chaudhuri, T., De, S., Bauer, W., Al Hadi, M., Sugitani, K., van Zuilen, M. A., Senda, R., Yamamoto, M., Raju, P.V.S., Ohta, T., Catuneanu, O., Mazumder, S., Saito, S., Shimooka, K., 2022. Paleoarchean surface processes and volcanism: Insights from the eastern Iron Ore Group, Singhbhum craton, India. Earth-Sci. Rev. 232, 104122. https://doi.org/10.1016/j.earscirev.2022.104122.

Mishra, S., Deomurari, M.P., Wiedenbeck, M., Goswami, J.N., Ray, S., Saha, A.K., 1999. 207Pb/206Pb zircon ages and the evolution of the Singhbhum Craton, eastern India: an ion microprobe study1This paper is dedicated to Prof. A.K. Saha, one of the senior co-authors, who passed away after submission of the paper.1. Precambrian Res. 93 (2), 139–151. https://doi.org/10.1016/S0301-9268(98)00085-0.

Misra, S., Moitra, S., Bhattacharya, S., Sivaraman, T.V., 2000. Archean Granitoids at the contact of Eastern Ghat Granulite Belt and Singhbhum-Orissa Craton, in Bhuban-Rengali Sector, Orissa, India. Gondwana Res. 3 (2), 205–213. https://doi.org/10.1016/S1342-937X(05)70097-6.

Misra, S., Sarkar, S.S., Ghosh, S., 2002. Evolution of Mayurbhanj Granite Pluton, eastern Singhbhum, India: a case study of petrogenesis of an A-type granite in bimodal association. J. Asian Earth Sci. 20 (8), 965–989. https://doi.org/10.1016/S1367-9120(02)00002-0.

Mitra, A., Dey, S., Zong, K., Liu, Y., Mitra, A., 2019. Building the core of a Paleoarchean continent: evidence from granitoids of Singhbhum Craton, eastern India. Precambrian Res. 335, 105436. https://doi.org/10.1016/j.precamres.2019.105436.

Mitra, A., Dey, S., Das, P., Zong, K., Liu, Y., Mitra, A., Gond, A.K., 2022. Time-space evolution of an ancient continent, a window to changing crustal architecture: Insights from granitoids of Singhbhum Craton, eastern India. Earth-Sci. Rev. 234, 104183. https://doi.org/10.1016/j.earscirev.2022.104183.

Moyen, J.-F., 2020. Archean granitoids: classification, petrology, geochemistry and origin. Geol. Soc. Lond. Spec. Publ. 489 (1), 15–49. https://doi.org/10.1144/SP489-2018-34.

Mukhopadhyay, J., Beukes, N.J., Armstrong, R.A., Zimmermann, U., Ghosh, G., Medda, R.A., 2008. Dating the Oldest Greenstone in India: a 3.51-Ga Precise U-Pb SHRIMP Zircon Age for Dacitic Lava of the Southern Iron Ore Group, Singhbhum Craton. J. Geol. 116 (5), 449–461. https://doi.org/10.1086/590133.

Mukhopadhyay, J., Ghosh, G., Zimmermann, U., Guha, S., Mukherjee, T., 2012. A 3.51 Ga bimodal volcanics-BIF-ultramafic succession from Singhbhum Craton: implications for Palaeoarchaean geodynamic processes from the oldest greenstone succession of the Indian subcontinent. Geol. J. 47 (2–3), 284–311. https://doi.org/10.1002/gj.1314.

Nebel, O., Capitanio, F.A., Moyen, J.F., Weinberg, R.F., Clos, F., Nebel-Jacobsen, Y.J., Cawood, P.A., 2018. When crust comes of age: on the chemical evolution of Archaean, felsic continental crust by crustal drip tectonics. Philos. Trans. Royal Soc. A: Math. Phys. Eng. Sci. 376 (2132), 20180103. https://doi.org/10.1098/rsta.2018.0103.

Nebel, O., Vandenburg, E.D., Capitanio, F.A., Smithies, R.H., Mulder, J., Cawood, P.A., 2024. Early Earth "subduction": short-lived, off-craton, shuffle tectonics, and no plate boundaries. Precambrian Res. 408, 107431. https://doi.org/10.1016/j.precamres.2024.107431.

Nelson, D.R., Bhattacharya, H.N., Thern, E.R., Altermann, W., 2014. Geochemical and ion-microprobe U–Pb zircon constraints on the Archaean evolution of Singhbhum Craton, eastern India. Precambrian Res. 255, 412–432. https://doi.org/10.1016/j.precamres.2014.09.024.

Olierook, H.K.H., Clark, C., Reddy, S.M., Mazumder, R., Jourdan, F., Evans, N.J., 2019. Evolution of the Singhbhum Craton and supracrustal provinces from age, isotopic and chemical constraints. Earth-Sci. Rev. 193, 237–259. https://doi.org/10.1016/j.earscirev.2019.04.020.

Pandey, O.P., Mezger, K., Ranjan, S., Upadhyay, D., Villa, I.M., Nägler, T.F., Vollstaedt, H., 2019. Genesis of the Singhbhum Craton, eastern India; implications

for Archean crust-mantle evolution of the Earth. Chem. Geol. 512, 85–106. https://doi.org/10.1016/j.chemgeo.2019.02.040.
Paton, C., Hellstrom, J., Paul, B., Woodhead, J., Hergt, J., 2011. Iolite: Freeware for the visualisation and processing of mass spectrometric data. J. Anal. At. Spectrom 26 (12), 2508–2518. https://doi.org/10.1039/C1JA10172B.
Pietranik, A.B., Hawkesworth, C.J., Storey, C.D., Kemp, A.I.S., Sircombe, K.N., Whitehouse, M.J., Bleeker, W., 2008. Episodic, mafic crust formation from 4.5 to 2.8 Ga: New evidence from detrital zircons, Slave craton, Canada. Geology 36 (11), 875–878. https://doi.org/10.1130/G24861A.1.
Reimink, J.R., Smye, A.J., 2024. Subaerial weathering drove stabilization of continents. Nature 629 (8012), 609–615. https://doi.org/10.1038/s41586-024-07307-1.
Rollinson, H., Chagondah, G., Hofmann, A., 2024. The late Archaean granite paradox: a case study from the Zimbabwe Craton. Precambrian Res. 410, 107491. https://doi.org/10.1016/j.precamres.2024.107491.
Rollinson, H.R., 1993. Using Geochemical Data: Evaluation, Presentation, Interpretation, 1st ed. Routledge, London.
Rubatto, D., 2002. Zircon trace element geochemistry: partitioning with garnet and the link between U–Pb ages and metamorphism. Chem. Geol. 184 (1), 123–138. https://doi.org/10.1016/S0009-2541(01)00355-2.
Saha, A.K., 1994. Crustal Evolution of Singhbhum-North Orissa, Eastern India. Memoir, p. 27.
Scharf, T., Kirkland, C.L., Barham, M., Yakymchuk, C., Puzyrev, V., 2023. Does zircon shape retain petrogenetic information? Geochem. Geophys. Geosyst. 24 (10), e2023GC011018. https://doi.org/10.1029/2023GC011018.
Sengupta, S., Paul, D.K., de Laeter, J.R., McNaughton, N.J., Bandopadhyay, P.K., de Smeth, J.B., 1991. Mid-Archaean evolution of the Eastern Indian Craton: geochemical and isotopic evidence from the Bonai pluton. Precambrian Res. 49 (1), 23–37. https://doi.org/10.1016/0301-9268(91)90054-E.
Sengupta, S., Corfu, F., McNutt, R.H., Paul, D.K., 1996. Mesoarchaean crustal history of the eastern Indian Craton: Sm-Nd and U-Pb isotopic evidence. Precambrian Res. 77 (1), 17–22. https://doi.org/10.1016/0301-9268(95)00042-9.
Shao, T., Xia, Y., Ding, X., Cai, Y., Song, M., 2019. Zircon saturation in terrestrial basaltic melts and its geological implications. Solid Earth Sci. 4 (1), 27–42. https://doi.org/10.1016/j.sesci.2018.08.001.
Siégel, C., Bryan, S.E., Allen, C.M., Gust, D.A., 2018. Use and abuse of zircon-based thermometers: a critical review and a recommended approach to identify antecrystic zircons. Earth-Sci. Rev. 176, 87–116. https://doi.org/10.1016/j.earscirev.2017.08.011.
Sláma, J., Košler, J., Condon, D.J., Crowley, J.L., Gerdes, A., Hanchar, J.M., Horstwood, M.S.A., Morris, G.A., Nasdala, L., Norberg, N., Schaltegger, U., Schoene, B., Tubrett, M.N., Whitehouse, M.J., 2008. Plešovice zircon — A new natural reference material for U–Pb and Hf isotopic microanalysis. Chem. Geol. 249 (1), 1–35. https://doi.org/10.1016/j.chemgeo.2007.11.005.
Söderlund, U., Patchett, P.J., Vervoort, J.D., Isachsen, C.E., 2004. The 176Lu decay constant determined by Lu–Hf and U–Pb isotope systematics of Precambrian mafic intrusions. Earth Planet. Sci. Lett. 219 (3), 311–324. https://doi.org/10.1016/S0012-821X(04)00012-3.
Spencer, C.J., Kirkland, C.L., Roberts, N.M.W., Evans, N.J., Liebmann, J., 2020. Strategies towards robust interpretations of in situ zircon Lu–Hf isotope analyses. Geosci. Front. 11 (3), 843–853. https://doi.org/10.1016/j.gsf.2019.09.004.
Sreenivas, B., Dey, S., Bhaskar Rao, Y.J., Vijaya Kumar, T., Babu, E.V.S.S.K., Williams, I. S., 2019. A new cache of Eoarchaean detrital zircons from the Singhbhum craton, eastern India and constraints on early Earth geodynamics. Geosci. Front. 10 (4), 1359–1370. https://doi.org/10.1016/j.gsf.2019.02.001.
Stern, R.A., Bodorkos, S., Kamo, S.L., Hickman, A.H., Corfu, F., 2009. Measurement of SIMS instrumental mass fractionation of Pb isotopes during Zircon dating. Geostand. Geoanal. Res. 33 (2), 145–168. https://doi.org/10.1111/j.1751-908X.2009.00023.x.
Topno, A., Dey, S., Liu, Y., Zong, K., 2018. Early Neoarchaean A-type granitic magmatism by crustal reworking in Singhbhum craton: evidence from Pala Lahara area, Orissa. J. Earth Syst. Sci. 127 (3), 43. https://doi.org/10.1007/s12040-018-0947-y.
Upadhyay, D., Chattopadhyay, S., Kooijman, E., Mezger, K., Berndt, J., 2014. Magmatic and metamorphic history of Paleoarchean tonalite–trondhjemite–granodiorite (TTG) suite from the Singhbhum craton, eastern India. Precambrian Res. 252, 180–190. https://doi.org/10.1016/j.precamres.2014.07.011.
Vernon, R.H., 1984. Microgranitoid enclaves in granites—globules of hybrid magma quenched in a plutonic environment. Nature 309 (5967), 438–439. https://doi.org/10.1038/309438a0.
Vernon, R.H., Etheridge, M.A., Wall, V.J., 1988. Shape and microstructure of microgranitoid enclaves: Indicators of magma mingling and flow. Lithos 22 (1), 1–11. https://doi.org/10.1016/0024-4937(88)90024-2.
Vervoort, J.D., Blichert-Toft, J., 1999. Evolution of the depleted mantle: Hf isotope evidence from juvenile rocks through time. Geochim. Cosmochim. Acta 63 (3), 533–556. https://doi.org/10.1016/S0016-7037(98)00274-9.
Vohra, C.P., Dasgupta, S., Paul, P.K., Bishui, P.K., Gupta, S.N., Guha, S., 1991. Rb-Sr chronology and petrochemistry of granitoids from the south-eastern part of the Singhbhum craton, Orissa. J. Geol. Soc. India 38 (1), 5–22.
Watkins, J.M., Clemens, J.D., Treloar, P.J., 2007. Archaean TTGs as sources of younger granitic magmas: melting of sodic metatonalites at 0.6–1.2 GPa. Contrib. Mineral. Petrol. 154 (1), 91–110. https://doi.org/10.1007/s00410-007-0181-0.
Watson, E.B., Harrison, T.M., 1983. Zircon saturation revisited: temperature and composition effects in a variety of crustal magma types. Earth Planet. Sci. Lett. 64 (2), 295–304. https://doi.org/10.1016/0012-821X(83)90211-X.
White, A.J.R., Chappell, B.W., 1977. Ultrametamorphism and granitoid genesis. Tectonophysics 43 (1), 7–22. https://doi.org/10.1016/0040-1951(77)90003-8.
White, R.W., Palin, R.M., Green, E.C.R., 2017. High-grade metamorphism and partial melting in Archean composite grey gneiss complexes. J. Metam. Geol. 35 (2), 181–195. https://doi.org/10.1111/jmg.12227.
Wiedenbeck, M., AllÉ, P., Corfu, F., Griffin, W.L., Meier, M., Oberli, F., Quadt, A.V., Roddick, J.C., Spiegel, W., 1995. Three natural zircon standards for u-TH-PB, LU-HF, trace element and REE analyses. Geostand. Newslett. 19 (1), 1–23. https://doi.org/10.1111/j.1751-908X.1995.tb00147.x.
Woodhead, J., Hergt, J., Shelley, M., Eggins, S., Kemp, R., 2004. Zircon Hf-isotope analysis with an excimer laser, depth profiling, ablation of complex geometries, and concomitant age estimation. Chem. Geol. 209 (1), 121–135. https://doi.org/10.1016/j.chemgeo.2004.04.026.
Woodhead, J.D., Hergt, J.M., 2005. A preliminary appraisal of seven natural zircon reference materials for in Situ Hf isotope determination. Geostand. Geoanal. Res. 29 (2), 183–195. https://doi.org/10.1111/j.1751-908X.2005.tb00891.x.
Wright, J.K., Basu, A.R., 2024. Vestiges of Earth's earliest depleted mantle reservoir. Geology. https://doi.org/10.1130/G51936.1.
Zoleikhaei, Y., Mazumder, R., Cawood, P.A., De, S., 2023. Paleo-Mesoarchean magmatism and sedimentation in the northern part of the Singhbhum Craton: evidence from zircon U-Pb-Hf, apatite U-Pb, and trace elements. Precambrian Res. 397, 107174. https://doi.org/10.1016/j.precamres.2023.107174.